Consequences of the Cretaceous west-dipping subduction in western North America

By

Wenbo Zhang

A thesis submitted in partial fulfillment of the requirements for the degree of

Master of Science

Department of Earth and Atmosphere Sciences

University of Alberta

Abstract

The westward growth of the North American Plate through amalgamation of the Cordillera terranes and North America Craton is a fundamental issue in tectonics. There is mounting evidence for Cretaceous westward subduction below the east side of the Cordillera, leading to terminal Cordillera-Craton collision; this contrasts with the long-held view of persistent east-dipping subduction on the west side. One key observation is the Omineca Magmatic Belt (OMB, 120-90 Ma) on the eastern side of the Cordillera. The OMB is associated with I-type plutons prior to 110 Ma, followed by an evolution to S-type granites. This is consistent with arc magmatism, where the mantle wedge progressively becomes contaminated with sediments as the Craton margin approached the plate margin.

We first examine the Craton response to subduction. As the strong Craton entered the trench, it experienced flexure, creating a topographic bulge. Flexural calculations for a 120 km thick elastic plate show that flexure would have induced tensile stresses in the deep Craton lithosphere 400-1200 km east of the subduction margin. The location of tensile stresses, the origination of the subduction margin, and the timing of Craton flexure correlate with the Central Cretaceous Kimberlite Corridor (CCKC, 115-92 Ma). This provides a novel explanation for kimberlite magmatism.

Next, we characterize additional observational constraints on Cretaceous westward subduction. First, we use 2D upper mantle scale numerical models to investigate the dynamics of subduction and Cordillera-Craton collision. Models show that following collision, the subducted oceanic plate detached. Break-off was accompanied a pulse of surface uplift, with greater uplift for a stronger cratonic lithosphere. Future work will involve how subduction and break-off

would be recorded in the OMB. Our studies constrain the feasibility of west-dipping subduction under the Cordillera during the Cretaceous.

Acknowledgements

I would like to express my sincere gratitude to my supervisors Dr. Stephen T. Johnston and Dr. Claire A. Currie for their mentorship, encouragement and patience throughout my graduate study. I am truly grateful to have had the privilege to work with you. My sincere thanks also goes to my supervisory committee: Dr. Larry Heaman for reviewing my thesis and providing valuable comments. I also appreciate Xiaowen Liu, Tachi, and Zhihong Pan and other friends for scientific discussions and fun-time. Thank you, Morgan, Merilie, Mike, Jared, and Ryan etc. for helping me in TA and introduce me the classic CRIBBAGE which I had so much fun with. Last but not least, I would thank my family for the encouragement and support throughout these many years when I am away from home.

Table of Contents

List of Figures

List of Tables

CHAPTER 1

1.1 Presentation of problem

Understanding continental-scale orogenic events that occurred more than 10-100 Ma ago is difficult. In the case of the Cordillera of western North America, interpretation of the orogen as a product of consistent eastward subduction beneath the west margin of the continent (e.g. Coney et al., 1980; DeCelles et al., 2009; Liu, 2014) is based on an array of data and models including petrological and geochemical analyses (Ducea, 2001; DeCelles et al., 2009), geodynamical modelling (Currie and Beaumont 2011; Liu and Currie 2016), and paleomagnetic and geobarometric studies (Harris et al., 1999; McCausland et al., 2006). There are, however, geological and geophysical observations that are difficult to reconcile with the model of consistent eastward-dipping subduction beneath the west margin of the continent. Some examples include: 1) Late Cretaceous arc-type magmas occur >700 km inboard of the inferred trench (English et al., 2003); 2) perhaps the largest volume magmatic belt in the entire orogen, the I- and S-type mid-Cretaceous Omineca Magmatic belt, is inferred to have been emplaced in the back-arc, a region that is normally characterized by small volume alkalic melts (Johnston, 2008); and 3) vertical 'slab walls' tomographically imaged beneath continental North America appear to have been constructed by west-dipping subduction of oceanic lithosphere that formerly lay west of, and was continuous with, continental North America (Sigloch and Mihalynuk, 2013). An alternative interpretation is that west-dipping subduction may have played a role in the development of the orogen (Johnston, 2008; Hildebrand, 2009; Sigloch and Mihalynuk, 2017). In the west-dipping subduction model, a Cordilleran ribbon continent or archipelago and cratonic Laurentia collided following the closure of an intervening oceanic domain (Johnston, 2008; Hildebrand, 2009; Sigloch and Mihalynuk, 2017).

The goal of my thesis is to test aspects of the westward subduction model. I provide two tests. In the first, forming Chapter 2, I test a model of west-dipping subduction to determine if it can explain coeval mid-Cretaceous magmatism both in the Cordillera and in cratonic Laurentia. The second test, forming Chapter 3, involves geodynamic modeling to determine if collision of a Cordilleran ribbon continent with cratonic Laurentia in response to closure of an intervening ocean basin by west-dipping subduction is consistent with available geological and geophysical constraints.

1.2 Method of Presentation

This thesis is presented as two stand-alone papers (Chapter 2 and 3). Chapter 1 and 4 provide an introduction including outlining the purpose of the study and a summary of conclusions and suggested follow-up studies, respectively. Both self-contained papers (Chapter 2 and 3) are co-authored by my supervisors, Dr. Stephen T. Johnston and Dr. Claire A. Currie. For both self-contained chapters (2&3), Dr. Stephen T. Johnston assisted with the design of the studies. Dr. Claire A. Currie assisted with setting up the numerical analyses and modeling.

CHAPTER 2. Kimberlite magmatism induced by west-dipping subduction of the North American Plate

2.1 Introduction

A key unresolved question regarding kimberlites is what triggers kimberlite magmatic events (Wyllie, 1980; McCandless, 1999; Heaman et al., 2004; Ault et al., 2015). Can kimberlites be ascribed to thermal or chemical processes at work within the mantle (intrinsic models), or do they result from external processes active within and/or acting upon the overlying lithosphere into which the kimberlites are emplaced (opportunistic models)? The temporal and geographic distribution of kimberlites and kimberlite provinces provide an important constraint on models of kimberlite magmatism.

Geochronological studies of North American kimberlite pipes have revealed a 4000 km long, north-south striking CCKC (Heaman et al., 2003, 2004) extending from Somerset, Nunavut (103-94 Ma), through Fort a la Corne, Saskatchewan (103-95 Ma) to Riley County, Kansas (~95 Ma)(Heaman et al., 2004; Kjarsgaard et al., 2017) (Fig. 2.1). How the CCKC was triggered is debated because the CCKC does not correspond to known mantle plume hotspot tracks(Heaman et al., 2003), lies outside regions of upwelling from the deep mantle (Torsvik et al., 2016), and lacks geochemical (trace element) evidence of any involvement of subduction-derived fluids (Kjarsgaard et al., 2017). The continental-scale CCKC parallels and lies east (inboard) of the Cordilleran Orogen of western North America, prompting Heaman et al. (2004) to suggest that the two may be linked. Here, we explore a tectonic linkage between the Cordilleran OMB and the CCKC.

2.1.1 Omineca Magmatic Belt and Central Cretaceous Kimberlite Corridor

The OMB (120-95 Ma) extends from Alaska, through the length of the Canadian

Cordillera into the conterminous United States (Fig. 2.1). It youngs from west to northeast, and

intrudes, from west to east, oceanic arc and pericratonic terranes of the Intermontane belt,

metamorphic continental rocks of the Omineca belt, and continental margin sequences of the

Foreland belt (Johnston, 2008; Hildebrand, 2014). Geochemical studies indicate that pre-110 Ma

plutons in the west are I-type, magnetite-bearing, oxidized, calc-alkaline intrusions. The 110-95

Ma plutons to the east (continentward) range from weakly oxidized magnetite- to reduced

ilmenite-bearing, mixed I- and S-type and voluminous peraluminous S-type granites (Hart et al.,

2004). From 95 to 90 Ma plutons forming the most inboard belt of plutons consist of small-

volume, zoned, locally silica-undersaturated, mafic to ultramafic, oxidized, magnetite bearing

stocks (Oldow et al., 1990; Hart et al., 2004; Johnston, 2008). OMB magmatism was coeval with

crustal shortening along foreland verging thrust faults and folds in the east, and dextral strike-slip

shearing in the west (Gordey and Anderson, 1993). Post-magmatic shortening primarily in the

Foreland belt gave rise to the latest Cretaceous Rocky Mountain and MacKenzie fold and thrust

belts (Price, 1981). Syn- and post-OMB crustal deformation was responsible for a maximum of

about 250 km of crustal shortening (Price, 1981).

Kimberlite magmatism in the CCKC was coeval with the latter stage of reduced, mostly

S-type OMB magmatism (Fig. 2.2). In addition to being coeval, the CCKC lies a consistent

distance east of the OMB (Fig. 2.1), varying from ~1000 km in the north to ~800 km in the

south. Restoring ~200-km-shortening at 50° N yields a constant OMB - CCKC distance of 1000

km.

We examine a west-dipping subduction model (Johnston, 2008; Sigloch and Mihalynuk, 2013; Hildebrand, 2014) to explain this temporal-spatial correlation. Our model challenges the long-held interpretation of the Cordillera as a product of long-lived east-dipping subduction at the west margin of the North American plate (Sharp, 1974; McCandless, 1999; Heaman et al., 2003; Currie and Beaumont, 2011). Instead it explains the OMB as a volcanic arc developed by west-dipping subduction beneath the east margin of the Cordillera of oceanic lithosphere continuous with and west of the North American continent. We suggest that the coeval CCKC was generated as a consequence of flexure and related extension at the base of the North American continent as it entered the trench adjacent to the Cordillera.
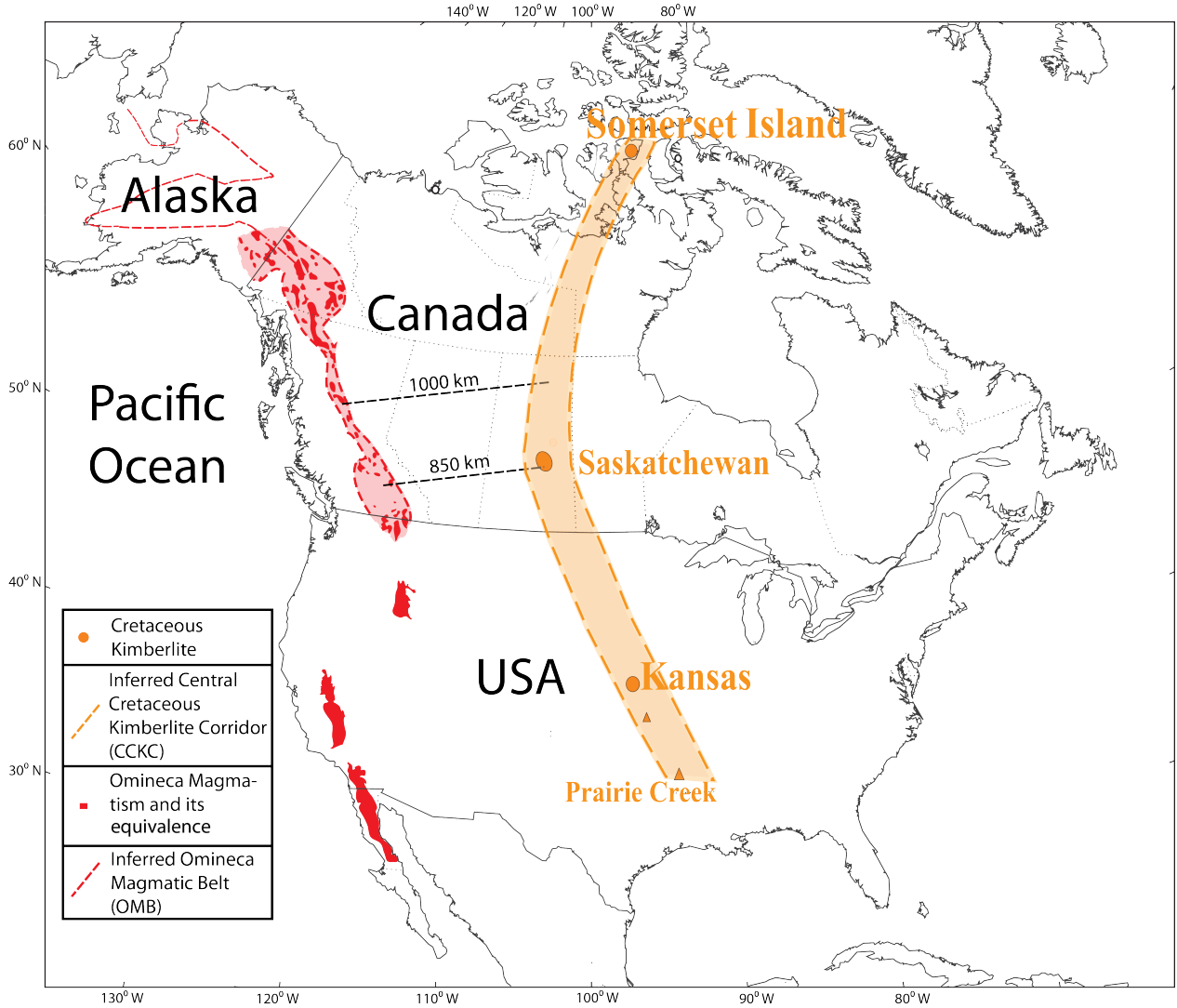
Figure 2.1. Geographic locations for OMB (red) and CCKC (orange) (Hart et al., 2004; Johnston, 2008; Hildebrand, 2014; Kjarsgaard et al., 2017)**.** Key kimberlite fields are labeled. Green line and blue patches are the OMB equivalents in Alaska and US, respectively.
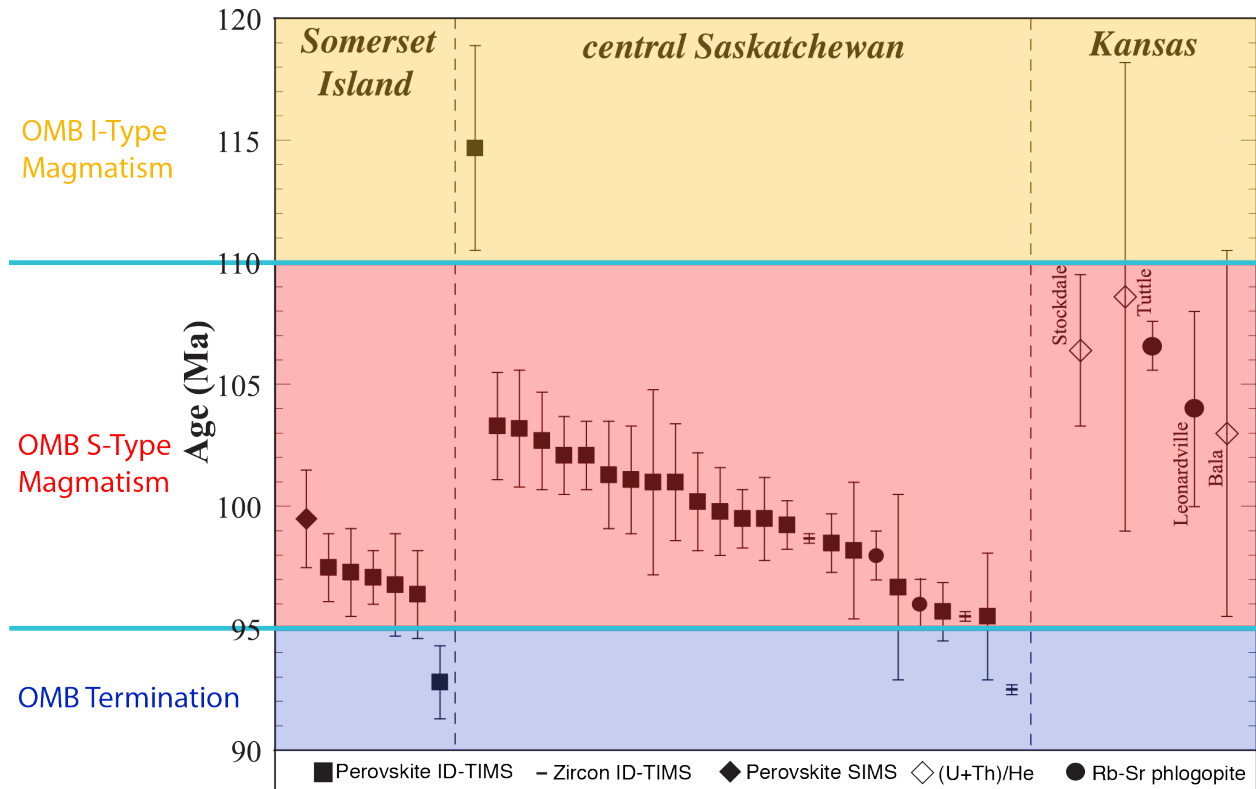
Figure 2.2. Age correlation between the OMB and the CCKC (Hart et al., 2004; Johnston, 2008; Kjarsgaard et al., 2017)**.** The coloured regions show the three stages of OMB magmatism, including I-type magmatism between 120 and 110 Ma (yellow), S- type magmatism 110-95 Ma (red), and termination at 95-90 Ma (purple). The symbols show the age determinations of the kimberlites using different methods, with 2σ uncertainty. Most of the kimberlites from Somerset, central Saskatchewan and Kansas are between 110-95 Ma, corresponding to OMB S-type magmatism.

2.1.2 A modern analogue of plate flexure

Subduction requires flexure of the lower plate lithosphere as it bends to enter the mantle. The elastic rigidity of the lithosphere results in a positive (upward) forebulge deflection of the downgoing plate oceanward of the trench, creating trench-perpendicular tensile stress in the upper part of the plate. Away (oceanward) from forebulge, the magnitude of deflection decreases and flexure results in trench-perpendicular compression in the uppermost plate and trench-perpendicular tensile stress in the lower part of the lithosphere.

Such flexure has been proposed to induce small-volume volcanism on oceanic plates (Hirano et al., 2006; Machida et al., 2017). The submarine 10 Ma and younger Petit-spot volcanoes, consisting of alkalic basalt, erupted through and onto Cretaceous lithosphere of the Pacific plate 600 km southeast (oceanward) of the Japan Trench. These have been explained as a result of plate flexure, where the fracturing and pressure reduction in the deep part of the plate enable upwelling of existing melt and small-volume decompressive melting at depths greater than 90 km (Hirano et al., 2006; Hirano, 2011; Pilet et al., 2016; Sato et al., 2018). This implies that the flexural tensile stress oceanward of the forebulge of the subducting plate is sufficient to all melts to migrate upward from underlying mantle.

We use this process as a modern analogue for the CCKC magmatism. We first test the interpretation that the Petit-spot volcanoes (Pilet et al., 2016) are attributable to plate flexure using a semi-infinite beam model (Watts, 2001) in order to constrain the state of stress in the lower part of the Pacific plate in the vicinity of the volcanoes. We then apply the model to a continental plate to determine if the CCKC magmatism can similarly be explained through plate flexure in response to the attempted westward subduction of the continent.

2.2 Flexural calculations

We plot (Fig. 2.3) the calculated deflection and stress distribution for an oceanic plate (Petit-spot volcanism) and a continental plate (CCKC). The flexural profile (deflection and stress field) primarily depends on flexural parameter (α) which in turn depends on the Young's modulus, Poisson's ratio, infill density, and elastic thickness (see Methods).

We select two sets of values for oceanic and continental plates, respectively (Table 2.1). The flexural wavelength (inverse of the flexural parameter) depends most strongly on the elastic thickness (T_e) of the plate and hence T_e is the main control on the deflection and stress

distribution. Here we use a T_e of 60 km for the oceanic plate, consistent with values for old oceanic lithosphere (Levitt and Sandwell, 1995; Turcotte and Schubert, 2002; Watts, 2001). An analysis of topography-gravity coherence shows that T_e for the North American Craton is between 80 to 150 km (Flück et al., 2003). We select 120 km for the Craton elastic thickness from flexural studies based on isopach map and topographic studies of the North American foreland basins (Beaumont, 1981; Painter and Carrapa, 2013).

Note that elastic thicknesses are typically less than lithospheric thicknesses from thermal and seismic considerations (Burov and Diament, 1995; Watts, 2001). Our flexure model is based on the assumption that the crust and uppermost mantle behave elastically during loading and unloading processes (Gunn, 1949; Burov and Diament, 1995; Watts, 2001), consistent with the overall cool thermal structure of the Craton region, where elastic behaviour is expected within both the crust and uppermost mantle and the two regions are mechanically coupled (Hyndman et al., 2009).

We focus on the stress distribution along the base of the elastic plate as this is key to understanding where mantle melts may enter the deep part of the plate (Hirano et al., 2006; Pilet et al., 2016). From the deflection curve, we choose the first node with no deflection as the reference point. This point is taken as the trench into which the lower plate was subducting. Our calculations show that tensile stresses on the lower surface of the elastic plate are found at 200-600 km and 400-1200 km relative to the reference point for oceanic and continental plates, respectively.
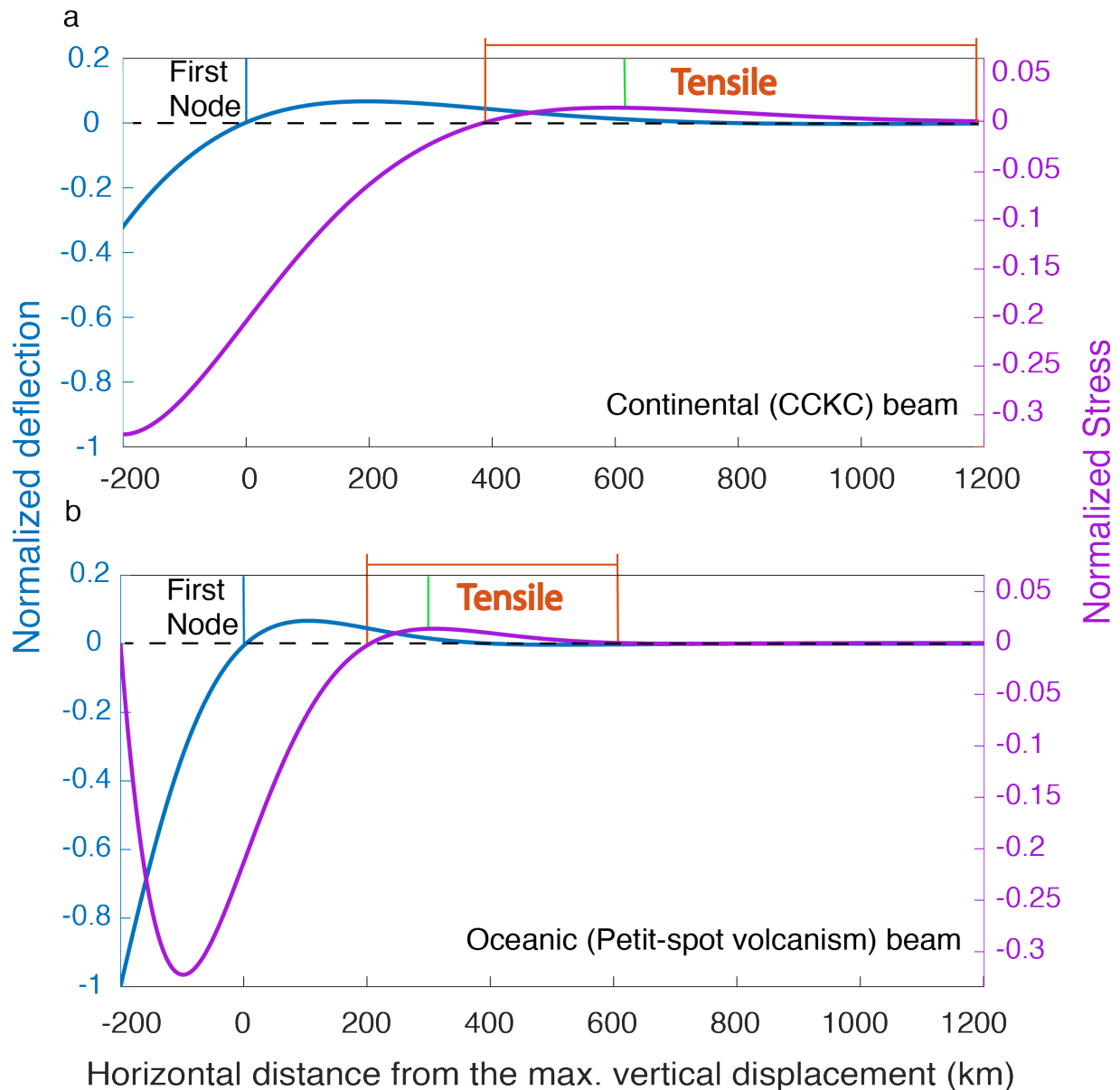
Figure 2.3. Normalized deflection and stress distribution plots for elastic flexure of (a) a continental plate and (b) an oceanic plate. Blue lines show the surface deflection; purple lines show the stress distribution on the bottom of the elastic plate (positive-tensile, negative-compressional). Blue marks represent the first node (no deflection). Red marks represent area under tensile stress. Green mark indicates the location of maximum tensile stress.

Using the above calculations, we first investigate the position of Petit-spot magmatism on the Pacific Plate based on our oceanic beam calculation (Fig. 2.4b). A convergence-parallel

cross-section view shows that the observed Petit-spot magmatism (found 600 km from the trench for the Pacific Plate (Hirano et al., 2006)) is located above the portion of the plate that is characterized by a tensile stresses along the elastic plate base and near the oceanward margin of the tensile region (Fig. 2.4b). Eruption of the Petit-spot volcanoes near the oceanward margin of the tensile stress domain may indicate exploitation of a suitably oriented local structure (e.g. orientation of the transform faults).

The OMB lies within the Cordilleran Orogen. Interpretation of the OMB as a volcanic arc attributable to westward subduction of (now-subducted) oceanic lithosphere that lay east of the OMB between the North American continent and the Cordillera (Johnston, 2008) implies that the suture/trench is cryptic. We assume a 300 km arc-trench gap, compatible with the observed global average for modern subduction zones (Syracuse et al., 2010) (Fig. 2.4a). After restoration of crustal shortening in the southern Canadian Rockies, the geographic location of the OMB is 1000 km west of the CCKC, placing the CCKC 700 km from the trench. Comparison with our flexural calculations show that the CCKC lies within the tensile stress domain which extends from 400 to 1200 km east of the trench (Fig. 2.4a). Our calculations also suggest that the CCKC was produced near the point at which the tensile stress acting across the base of the lower plate was near its maximum (~600 km east of the inferred trench).
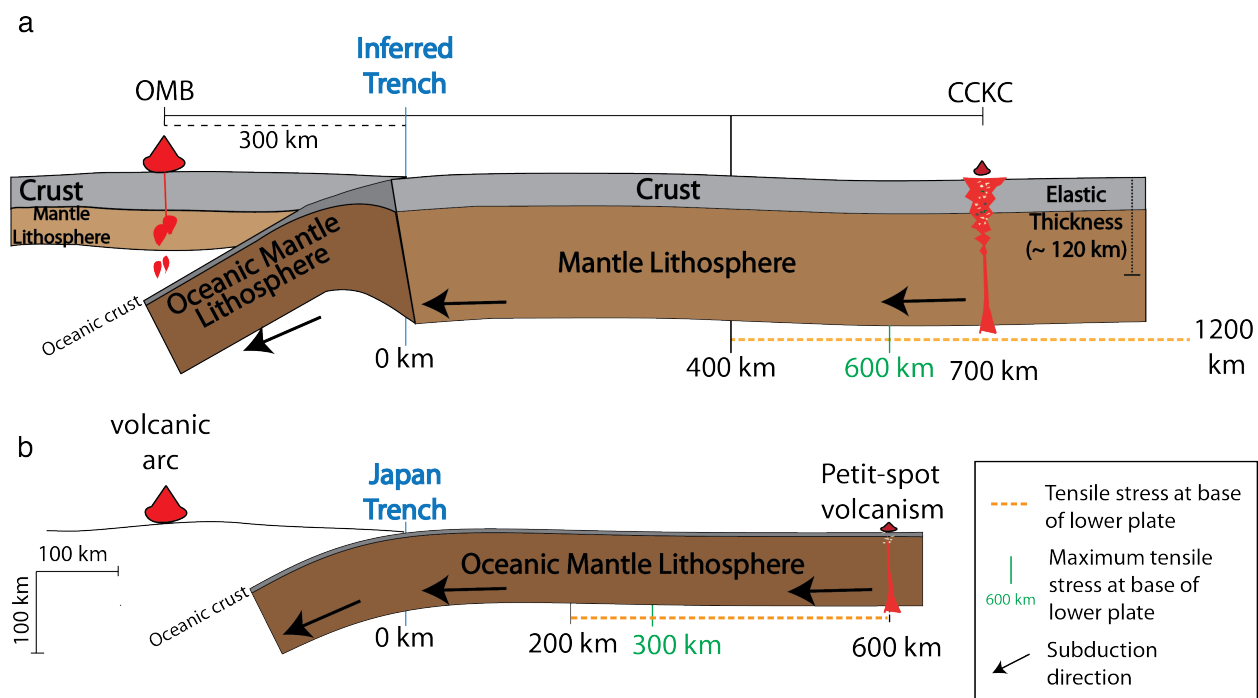
Figure 2.4. Convergence-parallel cross-sections for the spatial relationship between (a) the OMB to CCKC and (b) Petit-spot volcanism and subduction at the Japan trench.

2.3 Implications of correlation between the OMB and CCKC

We have demonstrated that eruption of the 10 Ma Petit-spot volcanoes onto the Cretaceous Pacific plate 600 km oceanward of the Japan trench is consistent with a tensile stress field attributable to forebulge-associated flexure of the subducting plate, in agreement with earlier interpretations (Hirano et al., 2006). Using the Petit-spot volcanoes as a modern analogue, we argue that the CKCC can be explained as a result of kimberlite eruption through the continental North American plate as it flexed during attempted westward subduction of the continent. In this model, the continent was attached to an oceanic plate which fully subducted, pulling the continent into the trench. Subduction of oceanic lithosphere continuous with, and west of, the North American continent is recorded by arc-magmatism in the OMB prior to 110 Ma. Entry of continental North America into the trench was recorded by a change in the nature of OMB magmatism (from I- to S-type magmatism, e.g. Cassiar batholith (Johnston, 2008)), and

by flexure of the lower plate continent giving rise to the coeval CCKC. The CCKC erupted within the tensile stress region in the lower part of the continent, within 100 km of the calculated location of the maximum tensile stress (Fig. 2.4).

Our study provides a coherent dynamical model to explain the temporal and spatial correlation between the Canadian OMB and the CCKC. Further work is needed to assess the OMB and CCKC for the Alaska and conterminous United States segments. Both regions show similar age OMB equivalents[7,8] but variable geographical distance relative to the CCKC (Fig. 2.1). Palinspastic restoration of the deformed belts is necessary to assess the spatial separation between the CCKC and the restored Cretaceous magmatic belts.

Although kimberlites are commonly assumed to characterize upper plates with deeply subducted slabs as the source of the volatiles (Sharp, 1974; McCandless, 1999), the correlation between distinct magmatic events with the Cordilleran orogen of western North America and the interval of kimberlite magmatism within the CCKC implies that at least the CCKC magmatism can be viewed as having been opportunistic and characterizing a subducting lower plate, and did not necessarily require intrinsic geochemical or thermal processes active deep within the mantle. Our model provides a mechanism to create tensile stresses in the lowermost continent, which may have triggered magmatism through either facilitating upward transport of existing melt, or by inducing decompressive melting, as proposed to explain low-volume magmatism outboard of modern subduction zone trenches (Hirano et al., 2006; Hirano, 2011). Even though kimberlite sources are usually formed in subcontinental lithospheric mantle (le Roex, 1986), asthenosphere (Griffin et al., 2000) or transition zone (Kjarsgaard et al., 2017), our model facilitates decompressive melting and migration of kimberlite magma from the asthenosphere due to lithospheric extension. Emplacement of the CCKC requires that kimberlite magmas traverse the

continental lithosphere, a vertical distance at ~200 km. The tensile stress at the plate bottom that

permitted decompressive melting cannot explain magma transit in the lithosphere, and suggests

that local structures within the plate are important for magma emplacement at the surface

(Kjarsgaard et al., 2017).

To summarize, the Cordilleran OMB and CCKC are temporally, spatially and genetically

related. The CCKC parallels and lies 1000 km east of the OMB, after restoring Cordilleran

shortening. The OMB is a magmatic arc that records west-dipping subduction beneath the

Cordilleran upper plate. The CCKC records flexure of the lower continental North American

plate upon its entry into the west-dipping subduction zone that separated the Cordillera from

North America. The Petit-spot magmatism on the Cretaceous Pacific plate 600 km oceanward of

the Japan trench is a modern analogue for this process. Our model provides insight into

flexurally induced magmatism of oceanic and continental plates, and a new mechanism for

diamondiferous kimberlite emplacement.

2.4 Methods

The purpose of our study is to determine the deflection and stress profile in response to

elastic plate flexure. The deflection mainly helps us define reference point along a horizontal

axis, based on which we can determine stress distribution. We use a semi-infinite beam model

(Timoshenko and MacCullough, 1935; Watts, 2001), where the elastic strength can be

characterized by the flexural parameter:

$$\alpha = \sqrt[4]{\frac{4\,E\,T_e^3}{12\,g(\rho_m - \rho_{infill})\,(1 - \nu^2)}} \qquad (2.1)$$

where α is flexural parameter, E is Young's modulus, T_e is the elastic thickness of the plate, ρ_m is

mantle density (~3300 kg/m^3), ρ_{infill} is density filled on top of the plate, ν is Poisson's ratio, and

g is gravity acceleration (9.81 m/s^2). The deflection at the top of the beam, as a function of horizontal distance (x) is given by:

$$W = \frac{2P_b * \lambda}{(\rho_m - \rho_{infill})g} e^{-\lambda x} \cos(\lambda x) = W_0\, e^{-\lambda x} \cos(\lambda x) \qquad (2.2)$$

The stress distribution along the bottom of the beam is:

$$S = -\frac{E\, 2P_b \lambda^3 T_e}{(1-\nu^2)(\rho_m - \rho_{infill})g} e^{-\lambda x} \sin(\lambda x) = S_0\, e^{-\lambda x} \sin(\lambda x) \qquad (2.3)$$

In equations (2.2) and (2.3), the P_b is the loading force acting on the free-end of the semi-infinite beam, and λ is the inverse of the flexural parameter. We define W_0 and S_0 to encompass all the variables that do not depend on x, and thus they are constants that modulate the amplitude of the stress and deflection profiles. For the stress distribution along the base of the elastic beam (equation (2.3)), positive and negative values represent extension and compression, respectively.

Table 2.1 gives the parameters used for the continental and oceanic plates in our calculations. Young's modulus describes ratio between uniaxial stress and strain. This commonly ranges between 0-100 GPa (Watts, 2001; Turcotte and Schubert, 2002), with oceanic plate being more mafic than continents and thus have a higher Young's modulus. Poisson's ratio describes the ratio between lateral and axial stresses and is ~0.25 for most rocks (Johnson and DeGraff, 1988; Watts, 2001; Turcotte and Schubert, 2002). We choose elastic thickness values based on studies from the Japan trench outer rise (Levitt and Sandwell, 1995; Turcotte and Schubert, 2002) and the Canadian Foreland basins (Beaumont, 1981). The infill density depends on the material overlying the flexed plate. We take this to be water for the oceanic plate (1000 kg/m^3) and sediments for the continent (2200 kg/m^3).

Table 2. 1. Parameters used in calculations

	Continents	Oceanic
Young's modulus (GPa)	70	80
Poisson's ratio	0.3	0.3
Elastic thickness (km)	120	60
Infill density (kg/m^3)	2200	1000
Mantle density (kg/m^3)	3300	3300
Flexural parameter (α, km)	250	130
Inverse of α (λ, km^{-1})	$3.95*10^{-9}$	$7.73*10^{-9}$

For a bending elastic beam, equation (2.2) expresses the deflection in the horizontal direction. We choose the point with no deflection as our reference point, corresponding to a horizontal distance of $\alpha\pi/2$ from maximum deflection. This reference point is taken as the trench for a subducting slab. On the stress profile (equation (2.3)), we identify 3 key points at distance of: $\alpha\pi$, $5\alpha\pi/4$, $2\alpha\pi$. The region between $\alpha\pi$ and $2\alpha\pi$ is the area where tensile stresses are predicted on the base of the elastic beam. The point $5\alpha\pi/4$ is the location of maximum tensile stress.

2.4.1 Normalization of stress and deflection plots

In Fig. 2.3, vertical axes for both stress and deflection are normalized and thus are dimensionless. In the normalization, all constants in equation (2.2) and (2.3) are equal to W_0 and S_0, respectively. Therefore, normalized values for deflection (W') and stress (S') are:

$$W' = \frac{W}{W_0} = e^{-\lambda x} \cos \lambda x \qquad (2.4)$$

$$S' = \frac{S}{S_0} = e^{-\lambda x} \sin \lambda x \qquad (2.5)$$

The reasons for normalization are (1) P_b (the line load) is a term that is not well constrained, and (2) W_0 and S_0 determine the amplitude of the plate deflection and stress but do not affect the wavelength. We are primarily interested in the lateral stress distribution in the direction of plate convergence (and thus orthogonal to the flexure axis) in our analysis as this affects the predicted horizontal location of magmatism (Petit-spot volcanism and the CCKC).

2.5 References

Ault, A.K., Flowers, R.M., and Bowring, S.A., 2015, Synchroneity of cratonic burial phases and gaps in the kimberlite record: Episodic magmatism or preservational bias? Earth and Planetary Science Letters, v. 410, p. 97–104, doi:10.1016/j.epsl.2014.11.017.

Bao, X., Eaton, D.W., and Guest, B., 2014, Plateau uplift in western Canada caused by lithospheric delamination along a craton edge: Nature Geoscience, v. 7, p. 830–833, doi:10.1038/ngeo2270.

Beaumont, C., 1981, Foreland basins: Geophysical Journal International, v. 65, p. 291–329, doi:10.1111/j.1365-246X.1981.tb02715.x.

Beaumont, C., Nguyen, M.H., Jamieson, R.A., and Ellis, S., 2006, Crustal flow modes in large hot orogens: Geological Society, London, Special Publications, v. 268, p. 91–145, doi:10.1144/GSL.SP.2006.268.01.05.

Bottrill, A.D., van Hunen, J., and Allen, M.B., 2012, Insight into collision zone dynamics from topography: numerical modelling results and observations: Solid Earth, v. 3, p. 387–399, doi:10.5194/se-3-387-2012.

Buiter, S.J.H., Govers, R., and Wortel, M.J.R., 2002, Two-dimensional simulations of surface deformation caused by slab detachment: Tectonophysics, v. 354, p. 195–210, doi:10.1016/S0040-1951(02)00336-0.

Burov, E.B., and Diament, M., 1995, The effective elastic thickness (Te) of continental
lithosphere: What does it really mean? Journal of Geophysical Research: Solid Earth, v.
100, p. 3905–3927, doi:10.1029/94JB02770.

Chase, C.G., Gregory-Wodzicki, K.M., Parrish, J., and Decelles, P.G., 1998, Topographic
history of the Western Cordillera of North America and Controls on Climate: Oxford
University Press,
https://books.google.ca/books?hl=en&lr=&id=HbamVUkDTLMC&oi=fnd&pg=PA73&d
q=cordillera+cretaceous+topography&ots=qek7hkWwn_&sig=KpQLIAujA18MC7z9Isg
YEZ1_f4I#v=onepage&q=cordillera%20cretaceous%20topography&f=false (accessed
October 2018).

Chen, Y., Gu, Y.J., and Hung, S.-H., 2018, A New Appraisal of Lithospheric Structures of the
Cordillera-Craton Boundary Region in Western Canada: Tectonics, v. 37, p. 3207–3228,
doi:10.1029/2018TC004956.

Chen, Y., Gu, Y.J., and Hung, S.-H. A New Appraisal of Lithospheric Structures of the
Cordillera-Craton Boundary Region in Western Canada: Tectonics, v. 0,
doi:10.1029/2018TC004956.

Coney, P.J., Jones, D.L., and Monger, W.H.J., 1980, Cordilleran suspect terranes: Nature, v. 288,
p. 329–333.

Currie, C.A., and Beaumont, C., 2011, Are diamond-bearing Cretaceous kimberlites related to
low-angle subduction beneath western North America? Earth and Planetary Science
Letters, v. 303, p. 59–70, doi:10.1016/j.epsl.2010.12.036.

DeCelles, P.G., 2004, Late Jurassic to Eocene evolution of the Cordilleran thrust belt and
foreland basin system, western U.S.A.: American Journal of Science, v. 304, p. 105–168,
doi:10.2475/ajs.304.2.105.

DeCelles, P.G., Ducea, M.N., Kapp, P., and Zandt, G., 2009, Cyclicity in Cordilleran orogenic
systems: Nature Geoscience, v. 2, p. 251–257, doi:10.1038/ngeo469.

Ducea, M., 2001, The California Arc: Thick Granitic Batholiths, Eclogitic Residues, Lithospheric-Scale Thrusting, and Magmatic Flare-Ups: GSA TODAY, p. 7.

Duretz, T., Gerya, T.V., and May, D.A., 2011, Numerical modelling of spontaneous slab breakoff and subsequent topographic response: Tectonophysics, v. 502, p. 244–256, doi:10.1016/j.tecto.2010.05.024.

Flück, P., Hyndman, R.D., and Lowe, C., 2003, Effective elastic thickness Te of the lithosphere in western Canada: Journal of Geophysical Research: Solid Earth, v. 108, doi:10.1029/2002JB002201.

Fullsack, P., 1995, An arbitrary Lagrangian-Eulerian formulation for creeping flows and its application in tectonic models: Geophysical Journal International, v. 120, p. 1–23, doi:10.1111/j.1365-246X.1995.tb05908.x.

Gleason, G.C., and Tullis, J., 1995, A flow law for dislocation creep of quartz aggregates determined with the molten salt cell: Tectonophysics, v. 247, p. 1–23, doi:10.1016/0040-1951(95)00011-B.

Gordey, S.P., and Anderson, R.G., 1993, Evolution of the Northern Cordilleran Miogeocline, Nahanni map area (105I), Yukon and Northwest Territories: Ottawa, Minister of Supply and Services Canada, Memoir / Geological Survey of Canada 428, 214 p.

Griffin, W.L., Pearson, N.J., Belousova, E., Jackson, S.E., van Achterbergh, E., O'Reilly, S.Y., and Shee, S.R., 2000, The Hf isotope composition of cratonic mantle: LAM-MC-ICPMS analysis of zircon megacrysts in kimberlites: Geochimica et Cosmochimica Acta, v. 64, p. 133–147, doi:10.1016/S0016-7037(99)00343-9.

Gunn, R., 1949, Isostasy extended: J. Geol., v. 57, p. 263–279.

Harris, M.J., Symons, D.T.A., Blackburn, W.H., and Hart, C.J.R., 1999, Paleomagnetic and geobarometric study of the Late Cretaceous Mount Lorne stock, southern Yukon Territory: v. 36, p. 11.

Hart, C.J.R., Goldfarb, R.J., Lewis, L.L., and Mair, J.L., 2004, The Northern Cordilleran Mid-Cretaceous Plutonic Province: Ilmenite/Magnetite-series Granitoids and Intrusion-related Mineralisation: Resource Geology, v. 54, p. 253–280, doi:10.1111/j.1751-3928.2004.tb00206.x.

Heaman, L.M., Kjarsgaard, B.A., and Creaser, R.A., 2004, The temporal evolution of North American kimberlites: Lithos, v. 76, p. 377–397, doi:10.1016/j.lithos.2004.03.047.

Heaman, L., kjarsgaard, B., and Creaser, R., 2003, The timing of kimberlite magmatism in North America: implications for global kimberlite genesis and diamond exploration: Lithos, v. 71, p. 153–184, doi:10.1016/j.lithos.2003.07.005.

Hildebrand, R.S., 2009, Did Westward Subduction Cause Cretaceous–Tertiary Orogeny in the North American Cordillera?, *in* Geological Society of America Special Papers, Geological Society of America, v. 457, p. 1–71, doi:10.1130/2009.2457.

Hildebrand, R.S., 2014, Geology, Mantle Tomography, and Inclination Corrected Paleogeographic Trajectories Support Westward Subduction During Cretaceous Orogenesis in the North American Cordillera: Geoscience Canada, v. 41, p. 207, doi:10.12789/geocanj.2014.41.032.

Hildebrand, R.S., and Whalen, J.B., 2017, The Tectonic Setting and Origin of Cretaceous Batholiths within the North American Cordillera: The Case for Slab Failure Magmatism and Its Significance for Crustal Growth: Geological Society of America, 123 p.

Hirano, N., 2011, Petit-spot volcanism: A new type of volcanic zone discovered near a trench: GEOCHEMICAL JOURNAL, v. 45, p. 157–167, doi:10.2343/geochemj.1.0111.

Hirano, N. et al., 2006, Volcanism in Response to Plate Flexure: Science, v. 313, p. 1426–1428, doi:10.1126/science.1128235.

Hyndman, R.D., and Currie, C.A., 2011, Why is the North America Cordillera high? Hot backarcs, thermal isostasy, and mountain belts: Geology, v. 39, p. 783–786, doi:10.1130/G31998.1.

Hyndman, R.D., Currie, C.A., Mazzotti, S., and Frederiksen, A., 2009, Temperature control of continental lithosphere elastic thickness, Te vs Vs: Earth and Planetary Science Letters, v. 277, p. 539–548, doi:10.1016/j.epsl.2008.11.023.

Ito, E., and Katsura, T., 1989, A temperature profile of the mantle transition zone: Geophysical Research Letters, v. 16, p. 425–428, doi:10.1029/GL016i005p00425.

Johnson, R.B., and DeGraff, J.V., 1988, Principle of Engineering Geology: Wiley, 512 p.

Johnston, S.T., 2008, The Cordilleran Ribbon Continent of North America: Annual Review of Earth and Planetary Sciences, v. 36, p. 495–530, doi:10.1146/annurev.earth.36.031207.124331.

Johnston, S.T., and Borel, G.D., 2007, The odyssey of the Cache Creek terrane, Canadian Cordillera: Implications for accretionary orogens, tectonic setting of Panthalassa, the Pacific superwell, and break-up of Pangea: Earth and Planetary Science Letters, v. 253, p. 415–428, doi:10.1016/j.epsl.2006.11.002.

Karato, S. -i., and Wu, P., 1993, Rheology of the Upper Mantle: A Synthesis: Science, v. 260, p. 771–778, doi:10.1126/science.260.5109.771.

Kjarsgaard, B.A., Heaman, L.M., Sarkar, C., and Pearson, D.G., 2017, The North America mid-Cretaceous kimberlite corridor: Wet, edge-driven decompression melting of an OIB-type deep mantle source: Geochemistry, Geophysics, Geosystems, v. 18, p. 2727–2747, doi:10.1002/2016GC006761.

Levitt, D.A., and Sandwell, D.T., 1995, Lithospheric bending at subduction zones based on depth soundings and satellite gravity: Journal of Geophysical Research: Solid Earth, v. 100, p. 379–400, doi:10.1029/94JB02468.

Liu, L., 2014, Constraining Cretaceous subduction polarity in eastern Pacific from seismic tomography and geodynamic modeling: Constrain Cretaceous subduction polarity: Geophysical Research Letters, v. 41, p. 8029–8036, doi:10.1002/2014GL061988.

Liu, S., and Currie, C.A., 2016, Farallon plate dynamics prior to the Laramide orogeny: Numerical models of flat subduction: Tectonophysics, v. 666, p. 33–47, doi:10.1016/j.tecto.2015.10.010.

Machida, S., Kogiso, T., and Hirano, N., 2017, Petit-spot as definitive evidence for partial melting in the asthenosphere caused by CO2: Nature Communications, v. 8, p. 14302, doi:10.1038/ncomms14302.

Mackwell, S.J., Zimmerman, M.E., and Kohlstedt, D.L., 1998, High-temperature deformation of dry diabase with application to tectonics on Venus: Journal of Geophysical Research: Solid Earth, v. 103, p. 975–984, doi:10.1029/97JB02671.

Magni, V., Allen, M.B., van Hunen, J., and Bouilhol, P., 2017, Continental underplating after slab break-off: Earth and Planetary Science Letters, v. 474, p. 59–67, doi:10.1016/j.epsl.2017.06.017.

McCandless, T.E., 1999, Kimberlites: Mantle Expressions of Deep-Seated Subduction: , p. 5.

McCausland, P.J.A., Symons, D.T.A., Hart, C., and Blackburn, W.H., 2006, Assembly of the northern Cordillera: New paleomagnetic evidence for coherent, moderate Jurassic to Eocene motion of the Intermontane belt and Yukon-Tananaterranes: v. 46, 147 p.

Monger, J.W.H., Price, R.A., and Tempelman-Kluit, D.J., 1982, Tectonic accretion and the origin of the two major metamorphic and plutonic welts in the Canadian Cordillera: Geology, v. 10, p. 70, doi:10.1130/0091-7613(1982)10<70:TAATOO>2.0.CO;2.

Oldow, J.S., Bally, A.W., and Avé Lallemant, H.G., 1990, Transpression, orogenic float, and lithospheric balance: Geology, v. 18, p. 991, doi:10.1130/0091-7613(1990)018<0991:TOFALB>2.3.CO;2.

Painter, C.S., and Carrapa, B., 2013, Flexural versus dynamic processes of subsidence in the North American Cordillera foreland basin: Geophysical Research Letters, v. 40, p. 4249–4253, doi:10.1002/grl.50831.

Pilet, S., Abe, N., Rochat, L., Kaczmarek, M.-A., Hirano, N., Machida, S., Buchs, D.M., Baumgartner, P.O., and Müntener, O., 2016, Pre-subduction metasomatic enrichment of the oceanic lithosphere induced by plate flexure: Nature Geoscience, v. 9, p. 898–903, doi:10.1038/ngeo2825.

Price, R.A., 1981, The Cordilleran foreland thrust and fold belt in the southern Canadian Rocky Mountains: Geological Society, London, Special Publications, v. 9, p. 427–448, doi:10.1144/GSL.SP.1981.009.01.39.

Pysklywec, R.N., and Beaumont, C., 2004, Intraplate tectonics: feedback between radioactive thermal weakening and crustal deformation driven by mantle lithosphere instabilities: Earth and Planetary Science Letters, v. 221, p. 275–292, doi:10.1016/S0012-821X(04)00098-6.

le Roex, A.P., 1986, Geochemical correlation between southern African kimberlites and South Atlantic hotspots: Nature, v. 324, p. 243–245.

Sato, Y., Hirano, N., Machida, S., Yamamoto, J., Nakanishi, M., Ishii, T., Taki, A., Yasukawa, K., and Kato, Y., 2018, Direct ascent to the surface of asthenospheric magma in a region of convex lithospheric flexure: International Geology Review, v. 60, p. 1231–1243, doi:10.1080/00206814.2017.1379912.

Sharp, W.E., 1974, A plate tectonic origin for diamond-bearing kimberlites: Earth and Planetary Science Letters, v. 21, p. 351–354, doi:10.1016/0012-821X(74)90173-3.

Sigloch, K., and Mihalynuk, M.G., 2013, Intra-oceanic subduction shaped the assembly of Cordilleran North America: Nature, v. 496, p. 50–56, doi:10.1038/nature12019.

Sigloch, K., and Mihalynuk, M.G., 2017, Mantle and geological evidence for a Late Jurassic−Cretaceous suture spanning North America: GSA Bulletin, doi:10.1130/B31529.1.

Syracuse, E.M., van Keken, P.E., and Abers, G.A., 2010, The global range of subduction zone thermal models: Physics of the Earth and Planetary Interiors, v. 183, p. 73–90, doi:10.1016/j.pepi.2010.02.004.

Timoshenko, S., and MacCullough, G.H., 1935, Elements of Strength of Materials: D. Van
Nostrand Company, Inc.

Torsvik, T.H., Steinberger, B., Ashwal, L.D., Doubrovine, P.V., and Trønnes, R.G., 2016, Earth
evolution and dynamics—a tribute to Kevin Burke (A. Polat, Ed.): Canadian Journal of
Earth Sciences, v. 53, p. 1073–1087, doi:10.1139/cjes-2015-0228.

Turcotte, D.L., and Schubert, G., 2002, Geodynamics: Cambridge University Press, 828 p.

Warren, C.J., Beaumont, C., and Jamieson, R.A., 2008, Formation and exhumation of ultra-high-
pressure rocks during continental collision: Role of detachment in the subduction
channel: Geochemistry, Geophysics, Geosystems, v. 9, p. n/a-n/a,
doi:10.1029/2007GC001839.

Watts, A.B., 2001, Isostasy and flexure of the lithosphere: Cambridge ; New York, Cambridge
University Press, 105–110 p.

Wyllie, P.J., 1980, The origin of kimberlite: Journal of Geophysical Research, v. 85, p. 6902,
doi:10.1029/JB085iB12p06902.

CHAPTER 3. Numerical models of the slab breakoff dynamics

3.1 Introduction

Numerical models provide an effective means for examination of the dynamics of subduction systems and the consequences of ocean closure. Such models can also be used to test tectonic models of collisional and accretionary orogens. The Cordilleran Orogen (Fig. 3.1) of western North America has commonly been interpreted as an accretionary orogen that developed in response to long-lived, east-dipping subduction beneath the west margin of the continent (Monger et al., 1982; DeCelles, 2004). An alternative interpretation is that the orogen developed due to collision between a Cordilleran ribbon continent or archipelago with cratonic North America in response to west-dipping subduction beneath the Cordillera in the Cretaceous. Here we numerically test the feasibility of the Cretaceous collisional model. We focus on the end-stages of subduction, as the subducting oceanic lithosphere draws the continental craton into the subduction zone. We investigate how the west margin of the cratonic North America evolves; the conditions that prevail during and after collision, including determining the fate of subducted slab; and how ocean closure, collision and post-collisional processes (e.g. slab breakoff) are recorded in the geological record.
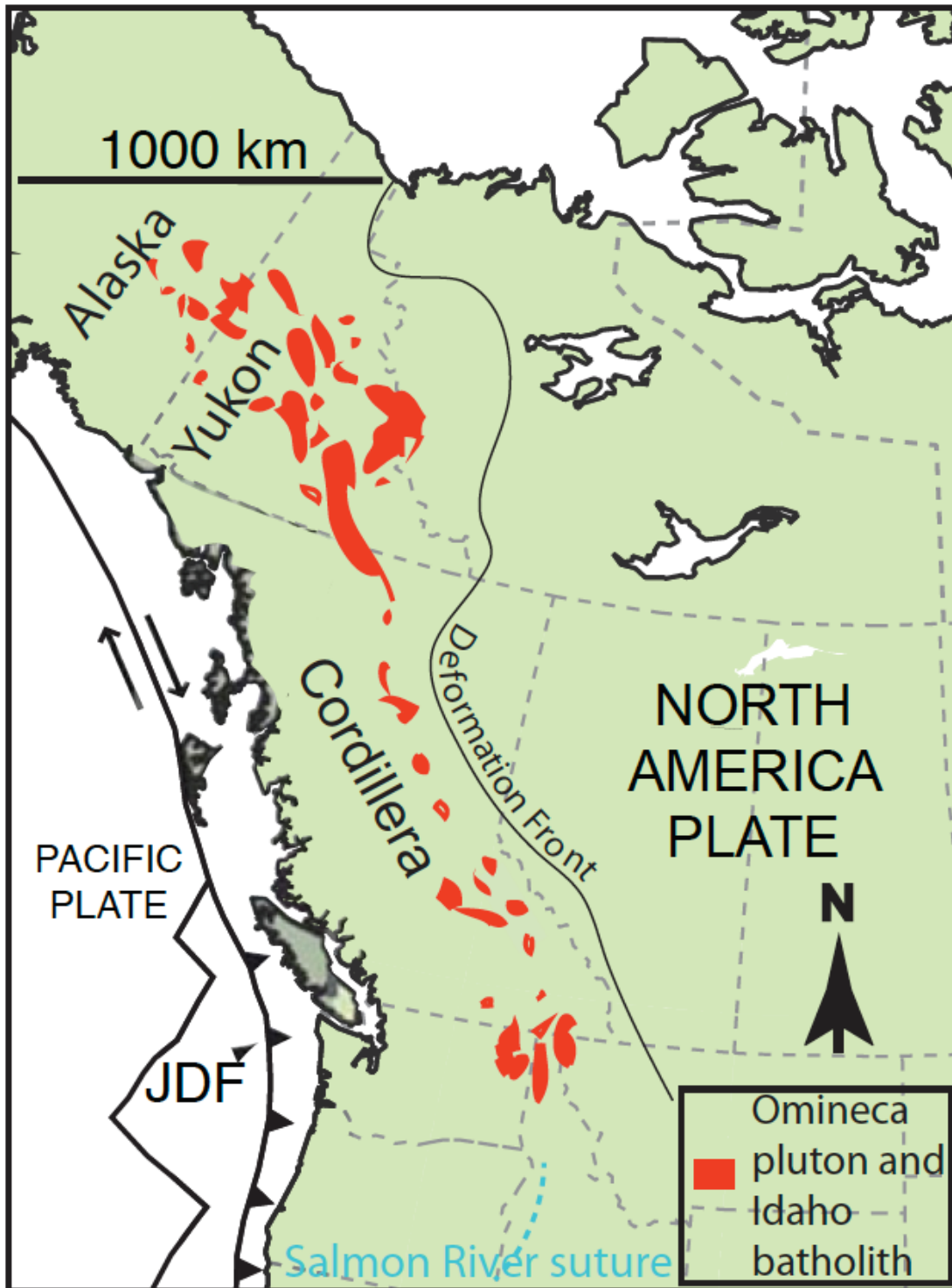
Figure 3.1. Map of the western and central North American plate showing the present-day tectonic plate margins. The deformation front separates the Cordillera and the North American Craton (modified from Currie and Beaumont, 2011).

3.2 Numerical methods

We first describe the model set up and then introduce the fundamental equations and numerical methods employed in our model. We next discuss the model material and thermal properties; and summarize the boundary conditions employed in the model (mechanical and thermal).

3.2.1 Model geometry

The models are two-dimensional, plane strain and incompressible cross-sections traversing a subduction zone from the Earth's surface down to the base of the upper mantle (~660 km depth). The SOPALE finite element code is used to solve the equations of mass, force balance, and energy conservation (Fullsack, 1995) and involves the implementation of an arbitrary Lagarangian-Eulerian (ALE) system. The Eulerian grid is fixed horizontally and can stretch vertically to record topographic responses. A Lagrangian mesh is used to track material properties through time. The code employed here has been previously applied to the study of the coupled thermal-mechanical behavior of the crust and upper mantle in the different tectonic settings, including convergent margin settings (Warren et al., 2008; Currie and Beaumont, 2011; Liu and Currie, 2016).

The model domain has a width of 3000 km and depth of 660 km from Earth's surface (Fig. 3.3). The model plane is taken to be parallel to the direction of the convergence between the Cordillera and the North American Cratpn. The Eulerian mesh includes 240 elements horizontally and 110 elements vertically. Elements are 12.5 km wide and are grouped in three horizontal layers, with 60 elements in the upper 180 km (3 km height), 20 elements in the middle 120 km (6 km height) and 30 elements in the lower 360 km (12 km height). The Lagrangian mesh, with a width of 5004 km and height of 660 km, and 9 times more nodes than the Eulerian mesh, starts 100 km left of the left boundary and 1904 km right to the right boundary of the Eulerian mesh. During the

model run, additional Lagrangian particles are injected to maintain a minimum number of particles in each Eulerian cell.

The model is divided into a continental Cordilleran plate to the west and a North American plate to the east. The North American plate is further divided into an oceanic domain that lies west of, and is continuous with, a more easterly continental domain (Fig. 3.4). The thickness of the Cordilleran lithosphere is 90 km, including a 24-km thick upper crust, a 12-km thick lower crust (36 km for crust) and a 54-km thick lithospheric mantle (Fig. 3.4). The horizontal dimension of the Cordilleran continent (1692 km) is wide enough for the oceanic subducting slab to descend without interference from the side boundaries.

The North American Plate includes a 1008 km wide oceanic domain and a more easterly, 300 km wide continental domain. We use a 90-km thick oceanic lithosphere (>100 Ma), including a 9-km thick oceanic crust and 81 km of lithospheric mantle. These values match the expected thickness of > 90 Ma old oceanic plate (Turcotte and Schubert, 2002). The continental crust is divided into upper (24 km) and lower (12 km) sections and is underlain by a 144-km thick lithospheric mantle for a total thickness of 180 km consistent with the cratonic character of the North American continent. Typical cratonic thermal lithospheric thickness is ~200 km from the thermal studies and seismic analysis (Hyndman and Currie, 2011).

29

Figure 3.2. Initial model geometry with boundary velocities and boundary temperatures. E stands for eclogite.

3.2.2 Modelling approach and governing equations

Here we summarize our modeling methodology. We employ arbitrary Lagrangian-Eulerian (ALE) application from Fullsack (1995). The SOPALE code calculates the mechanical flow of plastic-viscous materials in the creeping flow limit and the associated temperature field of the system (Fullsack, 1995). The thermal-mechanical evolution of the model is based on the assumptions of 2D plane strain (no strain orthogonal to the model plane) and incompressibility. There are two governing equations for material deformation, namely conservation of volume (mass conservation when compressible during metamorphic phase changes) (Warren et al., 2008) and force balance as follows:

$$\frac{\partial v_j}{\partial x_j} = 0 \tag{3.1}$$

$$\frac{\partial \sigma_{ij}}{\partial x_i} + \rho g = 0; \; i, j = 1,2 \tag{3.2}$$

where $x_{i,j}$ are spatial coordinates, v_i (following equations) and v_j are components of velocity, ρ is density, and g is gravitational acceleration. The associated stress tensor is:

$$\sigma_{ij} = -P\delta_{ij} + \sigma'_{ij} = -P\delta_{ij} + 2\eta_{eff}\dot{\varepsilon}_{ij} \tag{3.3}$$

where P is the mean stress, σ'_{ij} is the deviatoric stress tensor, η_{eff} is effective viscosity, δ_{ij} is the Kronecker delta (1 for i=j and 0 elsewise), and the strain rate tensor ($\dot{\varepsilon}_{ij}$) is:

$$\dot{\varepsilon}_{ij} = \frac{1}{2}\left(\frac{\partial v_i}{\partial x_j} + \frac{\partial v_j}{\partial x_i}\right) \tag{3.4}$$

The thermal evolution of the system is calculated using the energy balance equation:

$$\rho c_p \left(\frac{\partial T_K}{\partial t} + v_i \frac{\partial T_K}{\partial x_i}\right) = k \frac{\partial}{\partial x_i} \frac{\partial T_K}{\partial x_i} + \sigma'_{ij}\dot{\varepsilon}_{ij} + v_2 \alpha g T_K \rho + A \tag{3.5}$$

where c_p is specific heat, T_K is absolute temperature, t is time, k is thermal conductivity, α is thermal expansion coefficient per unit volume, v_2 is vertical velocity, and A is volumetric radioactive heat production. The second term on the right side of Equation 3.5 (deviatoric stress and strain rate tensors) corresponds to strain heating, assuming that the mechanical energy from deformation is converted to heat. The third term is a temperature correction for adiabatic heating for vertical velocity v_2.

Note that deformation is caused by material motions that result from internal buoyancy forces and mechanical and model boundary conditions (i.e., imposed plate convergence). The thermal and mechanical fields are coupled by strain heating term, material properties (see below), and by the redistribution of materials during deformation.

The governing equations (Equations 3.1, 3.2 and 3.5) are applied to the Eulerian mesh. Material deformation is tracked by using a Lagrangian mesh. The Eulerian velocity field is implemented to advect the Lagrangian mesh, allowing particles to redistribute in the model domain. The Lagrangian particles are then used to update the Eulerian material properties such as rheology and temperature-related density.

3.2.3 Material properties

All materials in the model have a viscous-plastic rheology. Frictional–plastic deformation follows a Drucker–Prager yield criterion:

$$(J_2')^{\frac{1}{2}} = P\sin\varphi_{eff} + C_0\cos\varphi_{eff} \tag{3.6}$$

where J_2' is the second invariant of the deviatoric stress tensor, P is the mean stress, C_0 is the

cohesion, and φ_{eff} is the effective internal angle of friction which takes pore fluid pressure into

account as follows: $P \sin\varphi_{eff} = P (1-\lambda) \sin\varphi,$ where λ is the pore fluid pressure ratio ($\lambda = P_f/P$,

where P_f is the pore fluid pressure) and φ is the dry coefficient of friction. Strain softening is

considered to decrease the φ_{eff} value linearly from 15° to 2° (Table 3.1). For the upper crusts,

the C_0 is 20 MPa. Other layers have C_0=0 MPa for cohesion. These values are based on those

used in earlier modeling studies (Pysklywec and Beaumont, 2004; Warren et al., 2008; Liu and

Currie, 2016).

When the deviatoric stress is below frictional-plastic yield stress, deformation becomes

viscous, following an effective viscosity (η_{eff}) given by:

$$\eta_{eff} = f(B^*)\dot{I}_2'^{(1-n)/2n} exp(\frac{Q+PV^*}{nRT_K}) \tag{3.7}$$

where f is a scaling factor, $\dot{I}_2$ is the second invariant of the strain rate tensor, R is the gas

constant (8.3145 J mol^{-1} K^{-1}), and B*, n, Q, and V* are the pre-exponential viscosity parameter,

stress exponent, activation energy, and activation volume, respectively. B* is a pre-exponential

factor converted from the pre-exponential factor (A*) obtained in uniaxial/triaxial laboratory

experiments (Currie and Beaumont, 2011); this conversion is needed as the models assume plane

strain conditions. The scaling factor (f) is used to linearly increase and decrease the effective

viscosity relative to the strength of the materials measured in the laboratory. This allows an

examination of the sensitivity of the models to reasonable changes in viscous strength owing to

variations in composition or water content between the model and laboratory materials, as well

as uncertainties in the laboratory parameters (Beaumont et al., 2006).

In our models, the upper continental crust follows a wet Black Hills quartzite rheology (Gleason and Tullis, 1995) with f=5, assuming that it is drier and less silicic than the laboratory wet quartzite. The oceanic crust and continental lower crust (including eclogites) use a dry Maryland diabase rheology (Mackwell et al., 1998). Mantle lithosphere (f=10) and sublithospheric mantle (f=1) have a wet olivine rheology (Karato and Wu, 1993) assuming the mantle lithosphere is dry and strong and sublithospheric mantle is hydrated and weak. A 'weak seed' is placed between the Cordillera and oceanic lithosphere, to allow subduction to be initiated (Fig. 3.2). The weak seed has a wet quartzite rheology with f=1 to ensure that it is weaker than the surrounding materials.

3.2.4 Thermal properties and density

Thermal parameters for each material follow those used in previous studies (Warren et al., 2008; Currie and Beaumont, 2011; Liu and Currie, 2016). These are given in Table 3.1. Radiogenic heat production (A) for upper and lower crusts (the Cordillera and the Craton) are 1.5 and 0.5 μWm^{-3}, respectively. There is no radiogenic heat production in either the oceanic crust or mantle lithosphere.

The thermal parameters are chosen to be consistent with the mechanical thickness of the lithosphere in each region. The temperature at the base of lithosphere corresponds to the intersection of a conductive geotherm with a mantle adiabat (1300°C potential temperature and 0.4°C/km adiabatic gradient). This constrains the lithospheric base temperature for oceanic and Cordilleran regions to be 1336°C and Cratonic region to be 1372°C.

For each continental region, the heat flow at the base of the mechanical lithosphere is

26.6 mW/m^2 and 68.6 mW/m^2 at the surface. For all materials, the thermal conductivity linearly increases from the values (2.25 or 3.935 W m^{-1} K^{-1}) to 66.8 W m^{-1} K^{-1} (to simulate the thermal convection) between 1336°C and 1372°C, corresponding to 90 and 180 km, respectively.

The density of all materials depends on temperature:

$$\rho(T)=\rho_0[1-\alpha(T-T_0)] \tag{3.9}$$

where ρ_0 is the reference density at temperature T_0 (°C) and α is the volumetric thermal expansion coefficient. Continental crusts materials are less dense than the oceanic crust (Table 3.1). The reference density for mantle materials is set to 3250 kg/m^3 at a temperature of 1336 °C.

We also factor in the temperature-pressure related metamorphic phase change to eclogite for the oceanic crust and continental lower crusts based on the phase diagram of Hacker et al. (2003). This phase change results in an increase in the density of the materials as they enter the eclogite stability field (Table 3.1). The phase change does not affect other material properties. In all models, the eclogite phase change is included for subducting oceanic crust (herein called eclogitization). For the continental lower crusts, we present tests that examine how eclogitization affects the dynamics of the models.

Table 3.1. Material properties in the model set-up

Parameters	Cordilleran Upper Crust	Cordilleran Lower Crust	Cordilleran Mantle Lithosphere	Oceanic Crust	Oceanic Mantle Lithosphere
Plastic rheology					
C_0 (MPa)	20	0	0	0	0
φ_{eff}	15-2°	15-2°	15-2°	15-2°	15-2°

Viscous rheology

f	5	0.1	10	0.1	10
A^* (Pa^{-n} s^{-1})	$8.57*10^{-28}$	$5.78*10^{-27}$	$3.91*10^{-15}$	$5.78*10^{-27}$	$3.91*10^{-15}$
B^*(Pa^{-n} s^{-1})^1	$2.92*10^{6}$	$1.91*10^{5}$	$1.92*10^{4}$	$1.91*10^{5}$	$1.92*10^{4}$
n	4	4.7	3	4.7	3
Q (kJ mol^{-1})	223	485	430	485	430
V^* (cm^3 mol^{-1})	0	0	10	0	10

Thermal parameters

k (Wm^{-1}K^{-1})	2.25	2.25	2.25	2.25	1.75
A (μWm^{-3})	1.5	0.5	0	0	0
c_p (J kg^{-1}K^{-1})^2	750	750	1250	750	1250

Density

ρ_0 (kg m^{-3})	2800	2900	3250	2950	3250
T_0 (°C)	200	500	1336	0	1336
Eclogite ρ_0 (kg m^{-3})^3	n/a	3350	n/a	3350	n/a
Eclogite T_0 (°C)	n/a	500	n/a	500	n/a
α (K^{-1})	$3*10^{-5}$	$3*10^{-5}$	$3*10^{-5}$	$3*10^{-5}$	$3*10^{-5}$

Table 3.1 Material properties in the model set-up (continued)

Parameters	Craton Upper Crust	Craton Lower Crust	Craton Mantle Lithospere	Sublithospheric Mantle	Weak Seed
Plastic rheology					
C_0 (MPa)	20	0	0	0	0
φ_{eff}	15-2°	15-2°	15-2°	15-2°	5-5°
Viscous rheology					
f	5	0.1	10	1	1
A^* (Pa^{-n} s^{-1})	$8.57*10^{-28}$	$5.78*10^{-27}$	$3.91*10^{-15}$	$3.91*10^{-15}$	$8.57*10^{-28}$
B^*(Pa^{-n} s^{-1})	$2.92*10^{6}$	$1.91*10^{5}$	$1.92*10^{4}$	$1.92*10^{4}$	$2.92*10^{6}$
n	4	4.7	3	3	4
Q (kJ mol^{-1})	223	485	430	430	223
V^* (cm^3 mol^{-1})	0	0	10	10	0

Thermal parameters					
k (Wm^{-1}K^{-1})	3.935	3.935	3.935	66.8	1.75
A (μWm^{-3})	1.5	0.5	0	0	0
c$_p$ (J kg^{-1}K^{-1})	750	750	1250	1250	1250
Density					
ρ_0 (kg m^{-3})	2800	2900	3250	3250	3250
T$_0$ (°C)	200	500	1336	1336	1336
Eclogite ρ_0 (kg m^{-3})	n/a	3350	n/a	n/a	n/a
Eclogite T$_0$ (°C)	n/a	500	n/a	n/a	n/a
α (K^{-1})	3*10^{-5}	3*10^{-5}	3*10^{-5}	3*10^{-5}	3*10^{-5}

[1] B* =2$^{(1-n)/n}$ 3$^{-(n+1)/2n}$ A$^{*-1/n}$. n is the pre-exponential stress exponent.
[2] c$_p$ is specific heat capacity.
[3] n/a represents that no eclogite is applied to the material.

3.2.5 Boundary conditions and modeling procedure

3.2.5.1 Mechanical boundary conditions

The mechanical boundaries constraining the physical model boundaries are shown in Fig. 3.3. The top boundary is a stress-free surface allowing for the growth of topography. The bottom boundary is a free-slip surface that prohibits vertical material transfer. On the sides, velocities are imposed on the entire thickness of lithosphere to induce plate convergence. As there is no observational evidence of the convergence rate between the North American and Cordilleran plate at 120-90 Ma, we use a convergence rate of 10 cm/yr. We later vary the convergence rate to test its effect on the subduction dynamics. In the model test, we set the velocity at the left boundary to 0 cm/yr (v_0) and impose convergence via an assigned velocity on the right boundary (V_a, influx). To maintain mass balance in the model domain, a uniform outflux is applied to the two side boundaries of the sublithospheric mantle (v_b), where the outflux velocity is:

$$v_a * h_0 = (h_1 + h_2 + 20) * v_b \qquad (3.10)$$

where h_0 is the thickness of cratonic lithosphere (180 km in this study), v_a is the plate

convergence rate, and $h_1 + h_2 + 20$ is the total length of the sublithospheric mantle for outflow

region. It is assumed that there is a 10-km transition zone between the base of the lithosphere and

sublithospheric mantle on each side (in total 20 km), where velocities linearly change from the

assigned lithosphere values (v_0 and v_a) to the outflux velocity (v_b). Since the side boundaries are

no-slip boundaries (Fig. 3.2), the vertical velocities are 0 cm/yr.

3.2.5.2 Thermal boundary conditions

The thermal boundary conditions are constrained as follows: (1) the top boundary is set to

the temperature of 0°C; (2) the bottom boundary of the box (660 km) has a fixed temperature of

1564°C, which is comparable to estimates of the temperature at the bottom of the transition zone

(Ito and Katsura, 1989); (3) the side boundaries of the sublithospheric mantle have no horizontal

heat transfer (i.e., insulating boundaries); and (4) the Cordillera and Craton lithospheres are

assigned conductive geotherms. Equations 3.11 and 3.12 are solved using the layers in the

continental lithosphere with surface heat flow (68.6 mW/m^2) and surface temperature (0°C) at

the top, and thermal conductivity and heat production from Table 3.1. These are calculated using

the steady-state heat equation, based on the boundary conditions of heat flow (Q_t) and

temperature (T_t) at the top surface:

$$T_{(z)} = T_t + \frac{Q_t}{k_{\delta z}} \delta z - \frac{A_{\delta z}}{2 k_{\delta z}} \delta z^2 \qquad (3.11)$$

where δz is the layer interval (counting from the corresponding interval surface to downward), and the layer intervels are the layer domains in Fig. 3.2. T_t is the temperature at the top of the layer (e.g. surface is 0°C), Q_t is the heat flow at the top of the layer, $k_{\delta z}$ is the thermal conductivity at the interval of δz, and $A_{\delta z}$ is the radiogenic heat production at the interval of δz. To calculate the heat flow at the bottom of the layer, the equation is given as:

$$Q_b = Q_t - A_{\delta z}\,\delta z \qquad (3.12)$$

The initial thermal structure of the model domain is calculated using the assigned thermal boundary conditions and material thermal properties. In these recurring calculations, the craton mantle lithosphere has a thermal conductivity of 3.935 $\text{Wm}^{-1}\text{K}^{-1}$ so that its starting thermal structure is consistent with the 180-km thick lithosphere. For the Cordilleran mantle lithosphere, the initial thermal conductivity is 2.25 $\text{Wm}^{-1}\text{K}^{-1}$, which correlates to 90-km thick lithosphere.

3.2.5.3 Modeling phases

The numerical model runs are divided into three phases. In Phase 1, material properties and boundary conditions are used to (1) establish the initial 2D thermal structure for the model domain and (2) ensure isostatic balancing. In this phase, there are no horizontal inflow velocities and thus no convergence. At the end of this phase the North American oceanic and cratonic lithospheres forms a ~4 km deep oceanic basin while the Cordillera is at the sea level.

Phase 2 and 3 model plate convergence, subduction and cratonic collision with the Cordillera over a time of 30 Ma. During these phases, a time step of 2000 years is used. These time steps ensure that the model can run stably in a constrained time of period. In Phase 2 (Fig. 3.3a), subduction is initiated by applying a velocity of v_a = 5 cm/yr to the Craton side boundary,

while the Cordillera boundary has $v_0 = 0$ cm/yr (i.e., the Cordillera is stationary). This induces

plate convergence, and subduction initiation is aided by the presence of an inclined weak seed in

the oceanic mantle lithosphere at the boundary of the oceanic and Cordilleran plates (Fig. 3.2).

This phase involves 500 km of convergence over 10 Ma and leads to the establishment of a

subduction zone. At the end of this phase, the west edge of the cratonic lithosphere is located 500

km east of the trench.

The numerical experiments start at this point and correspond to Phase 3 of the model run.

At the start of Phase 3 (Fig. 3.3b), the plate convergence rate is increased to 10 cm/yr (v_a).

Convergence brings the cratonic lithosphere into the subduction zone, with collision occurring 5

Myr after the start of Phase 3. After another 300 km of 10 cm/yr convergence, subduction (and

convergence) is stopped, reflecting our assumption that entry of continental lithosphere into the

subduction zone would lead to a cessation of subduction. We then observe the behaviour of the

oceanic slab. Cessation of convergence also minimizes the effect of shear between the slab and

the base of the model (660 km).

We convert our model time to geological time based on the I- to S- type magmatism of

Omineca Magmatic Belt, implying that continental collision occurred at 110 Ma (Johnston,

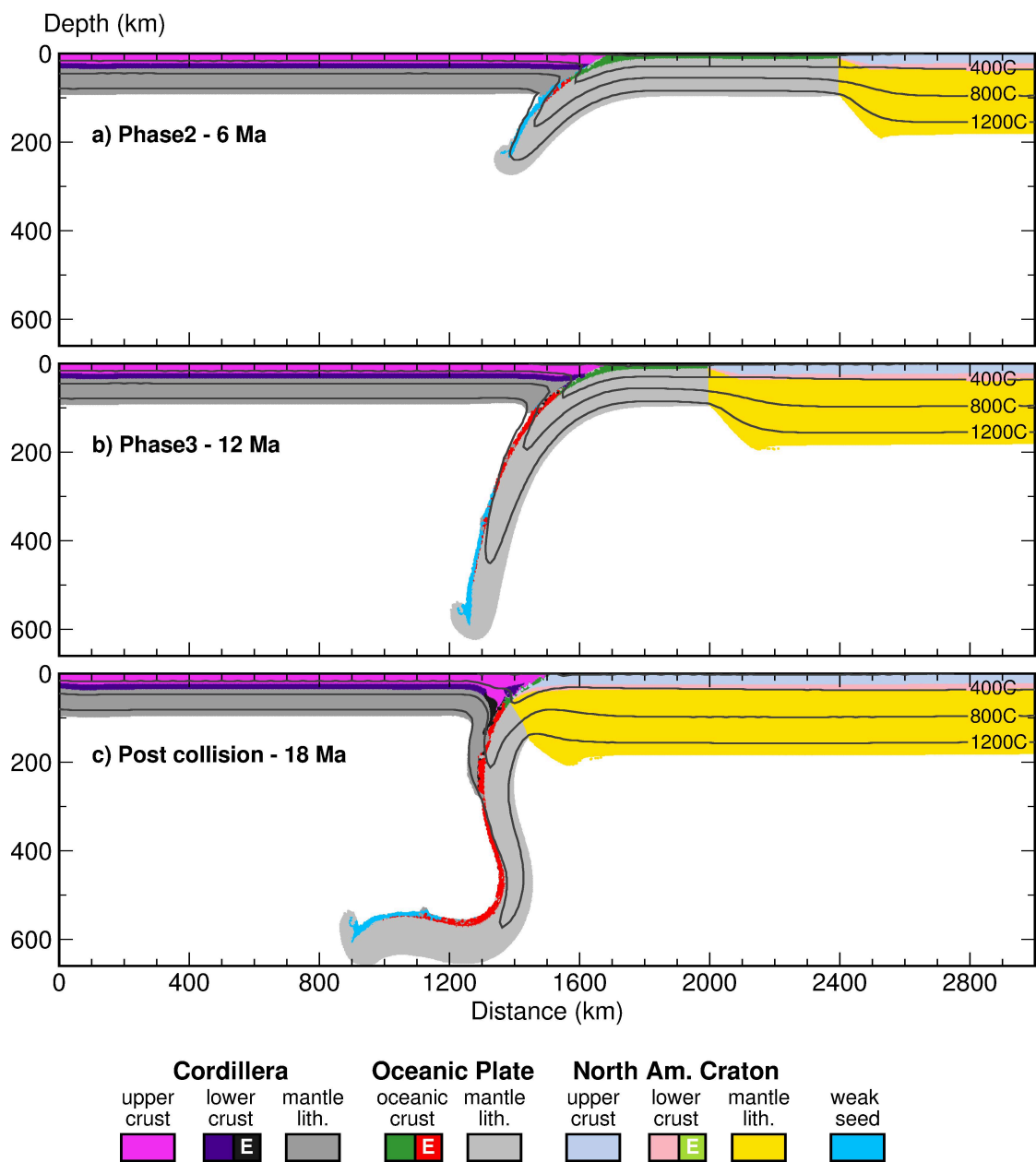2008). Therefore, in our model, continental collision is calibrated to 110 Ma.

Figure 3.3. Model geometry illustrating the key phases in a model run. a) Phase 2, subduction initiated. b) Start of the Phase 3, after the development of steeply dipping subduction (500 km of convergence in Phase 2). c) An example of a model after 8 Ma of Phase 3 (1800 km of convergence), showing continental collision with 300-km crustal shortening.

3.3 Numerical model results

We conduct a series of experiments in Phase 3 to determine the implications of west-dippping subduction, the geological ramifications of collision, and the fate of the subducted oceanic lithosphere following collision. We look at the significance of: a) variations in the strength of lithospheric mantle, b) eclogitization of both continental lower crusts and variations in the density of the cratonic lithospheric mantle, and c) variations in convergence rate. Below, we examine each of these factors individually and determine a preferred model. Based on geological evidence (see Discussion), we take 110 Ma as the time of continental collision. In our models (Fig. 3.5-3.9, Table 3.2), we show an 1100 km wide section focused on the collision zone; the full width of the model is 3000 km. Our observations are mainly focused on the fate of the subducted slab (e.g. Fig. 3.5b)

3.3.1 Reference model

We first set up a reference model (Model-R), using the material properties given in Table 3.1. Subsequent models investigated parameter variations relative to the reference model. At the end of convergence, the oceanic slab is still attached to the cratonic North America (Fig. 3.4). In the trench area, part of the oceanic crust forms an off-scrapped accretionary wedge accreted to the Cordilleran upper plate. The Cordilleran lower crust has been exhumed at the subducting contact (Fig. 3.4). When the slab interacts with the bottom boundary of the model, it is deflected. In this model, the subducted oceanic slab remains attached to the continental lower plate long after collision and the cessation of convergence. The lower plate oceanic and cratonic lithospheric mantles employed in this model are strong (f=10) and likely explains the lack of slab break-off. For the following models, we test parameters affecting the fate of the subducted slab.
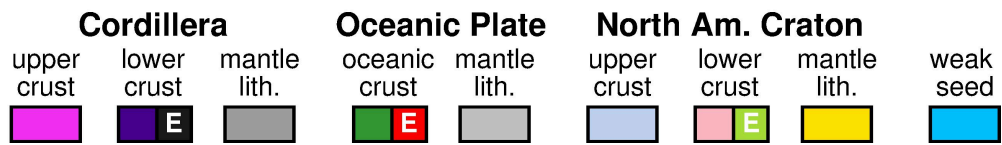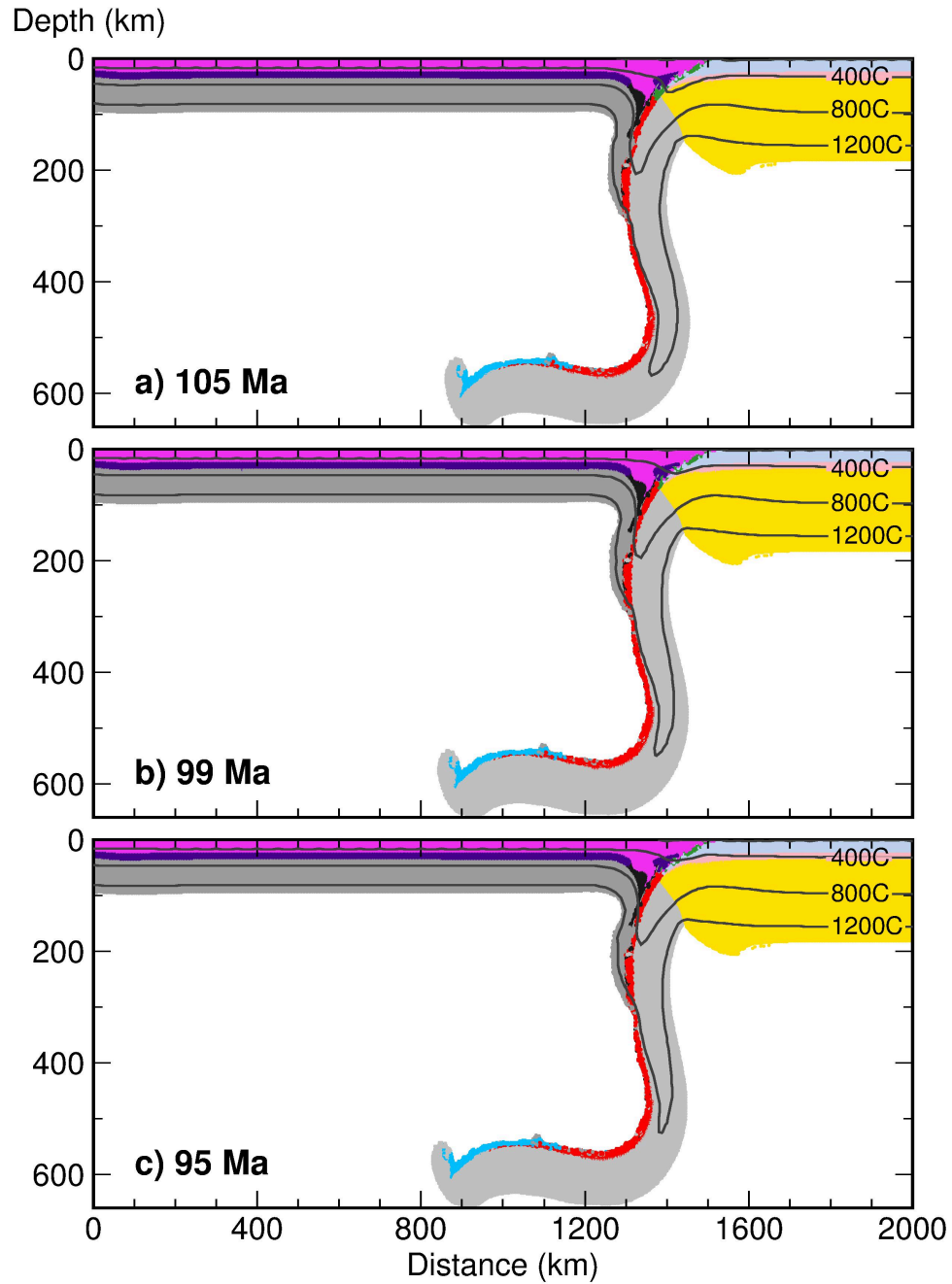
Figure 3.4. Evolution of the reference model run since the continental collision. E in the legend indicates eclogite.

Table 3.2. List of numerical models of west-dipping subduction. Note that each color represents corresponding figures and the model parameter that is being compared. ML=mantle lithosphere. R=reference model

Model	Lower crust eclogitization	Convergence rate	Continental ML strength	Oceanic ML strength	Continental ML density	Figure
R	y	10	10	10	3250	3.4, 3.5, 3.6, 3.7
1	y	10	10	1	3250	3.5, 3.8, 3.9
2	y	10	1	10	3250	3.6
3	n	10	10	10	3250	3.7
4	y	10	10	1	3210	3.8
5	y	5	10	1	3250	3.9
Preferred	y	5	2.5	5	3250	3.10

3.3.2 Mantle lithosphere strengths

Here we consider variations in the strength of the lithospheric mantle for both the continental and oceanic lithospheres. Effective viscosity (equation 3.7) plays an important role in our viscous-plastic model. In the model set up, we vary the scaling factor (f) to simulate the material strength in oceanic and continental lithospheres (e.g. f=10 is strong). In the reference model (f=10 for both continental and oceanic mantle lithosphere), there is no indication of slab breakoff in the model time.

In this comparison (Model-1), we examine the role of the oceanic lithosphere by employing a weak oceanic lithospheric mantle (f=1). Model-1 (Fig. 3.5b) indicates that the weak oceanic lithospheric mantle (f=1) leads to necking (stretching of the slab) beginning at 105 Ma (5 Myrs after collision) and break-off at ~99 Ma (11 Myrs after collision) (Fig. 3.5b). Detachment occurs at depth of ~280 km, leaving a ~200-km long slab of oceanic lithosphere attached to the cratonic North American lithosphere.
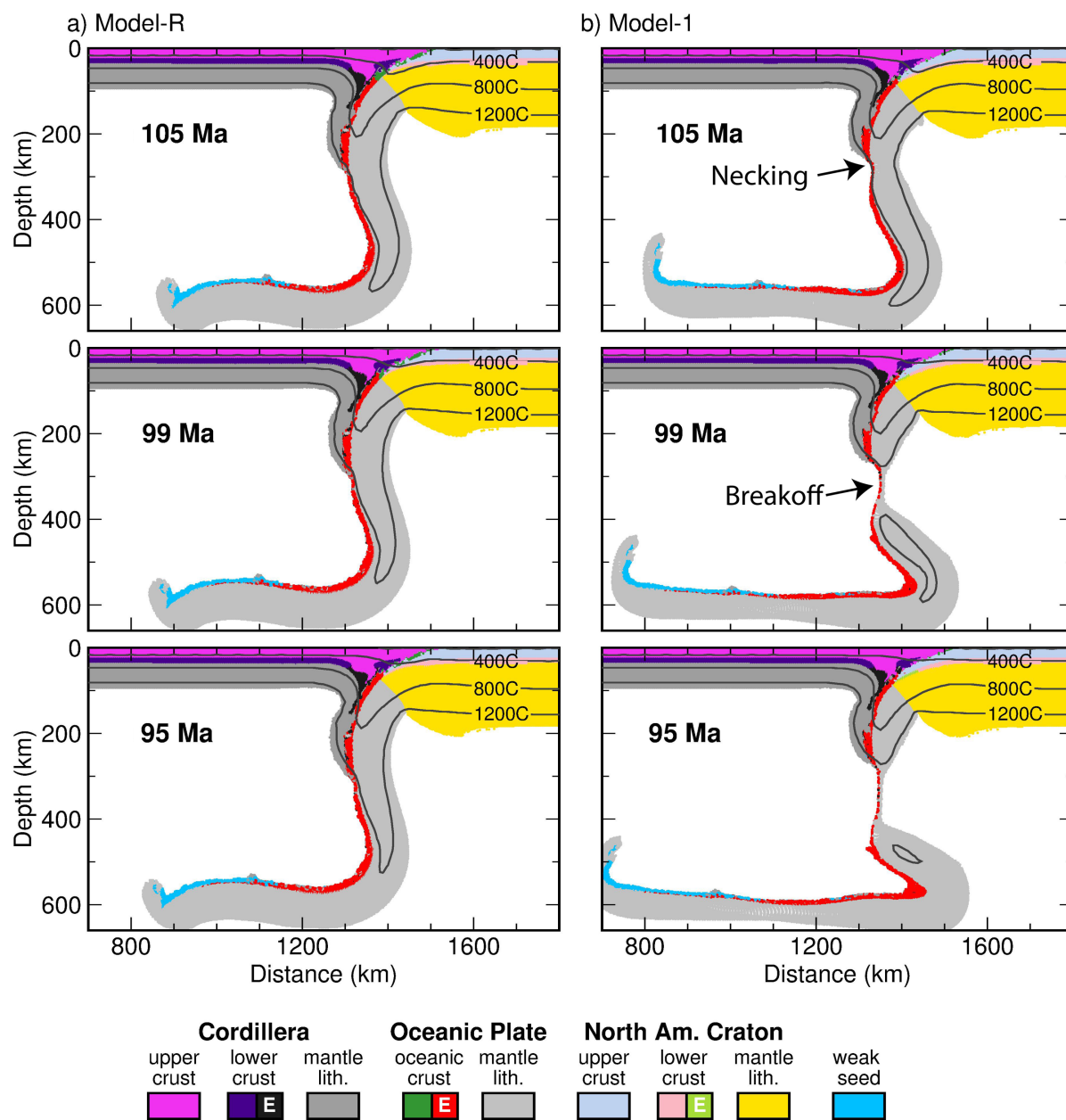
Figure 3.5. Oceanic mantle lithosphere strength comparison. a) Model-R, oceanic ML strength (f) =10. b) Model-1, oceanic ML strength (f) =1. E=eclogite in the legend.

In the second comparison, we vary the continental lithospheric mantle scaling factor (e.g. f=1). For simplicity, we assume that the lithospheric mantle strength of the lower cratonic North America and the Cordillera are equal. In Fig. 3.6b, the strength scaling factor for the continental lithospheric mantle is reduced to f=1. With the reduced strength, the oceanic slab starts to detach

from the weak craton mantle lithosphere at 99 Ma, 11 Myrs after collision (Fig. 3.6b). It rapidly breaks off, leaving a sharp vertical boundary between the upper Cordilleran and lower cratonic North American plates. After slab breakoff, the oceanic slab (mantle lithosphere f=10) sinks gradually and flattens at the base of the model domain (above 660 km). Our results indicate that a weaker cratonic lithospheric mantle (with a strong oceanic lithosphere) yields slab breakoff, resulting in a sharp boundary between the opposing upper and lower plates.
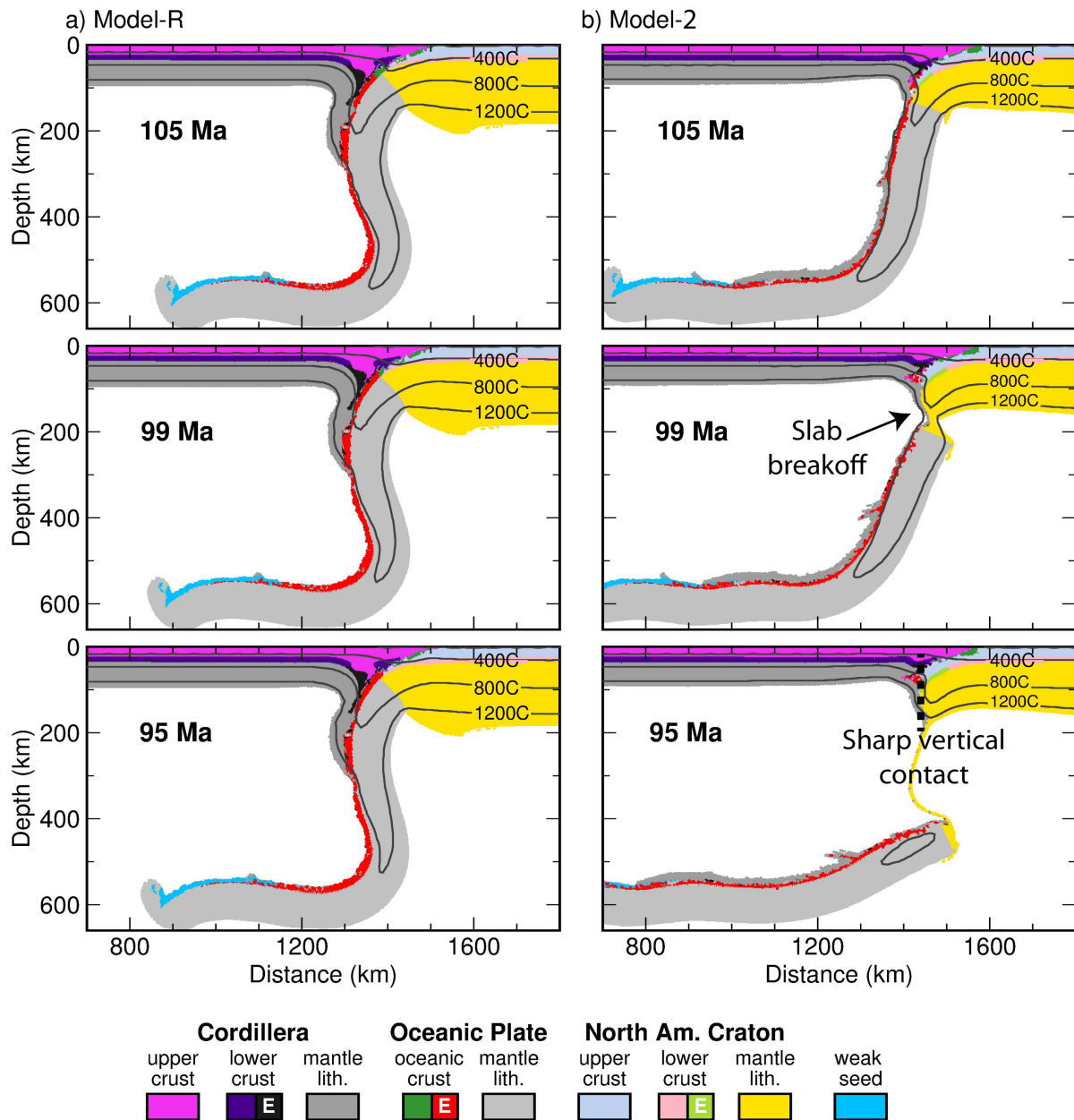
Figure 3.6. Continental mantle lithosphere strength comparison. a) Model-R, continental ML strength (f) =10. b) Model-2, Continental ML strength (f) =1. E=eclogite in the legend.

3.3.3 Variations in density

Here we examine density variation in the continental lower crust and lithospheric mantle. In these models, we keep the densities of the oceanic lithosphere layers the same as in the reference model.

a) Densification (eclogitization) of the continental lower crust

We first examine the effect of eclogitization of the continental lower crust. In the reference model, the continental lower crusts (2900 kg/m^3) are eclogitized to a density of 3350 kg/m^3 (both at 500°C) based on the eclogitization phase change from Hacker et al. (2003). In Model-3, the lower crustal density does not change. Note that, we tend to simplify our legend label in our figures. Therefore in Fig. 3.7, all plots show where the continental lower crust is within the eclogite stability field but Model-3 has no density effect from the eclogitization. Hereafter we define "densification" as an increase in density and no density change as "no densification" (Liu and Currie, 2016).

Fig. 3.7 shows that densification of the continental lower crusts yields no significant effect on the fate of the subducting slab. Densification of the continental lower crust (Model-R) facilitates separation of the Cordilleran continental crust and lithospheric mantle. It is likely that the eclogitized lower crust descends due to higher density of eclogite.
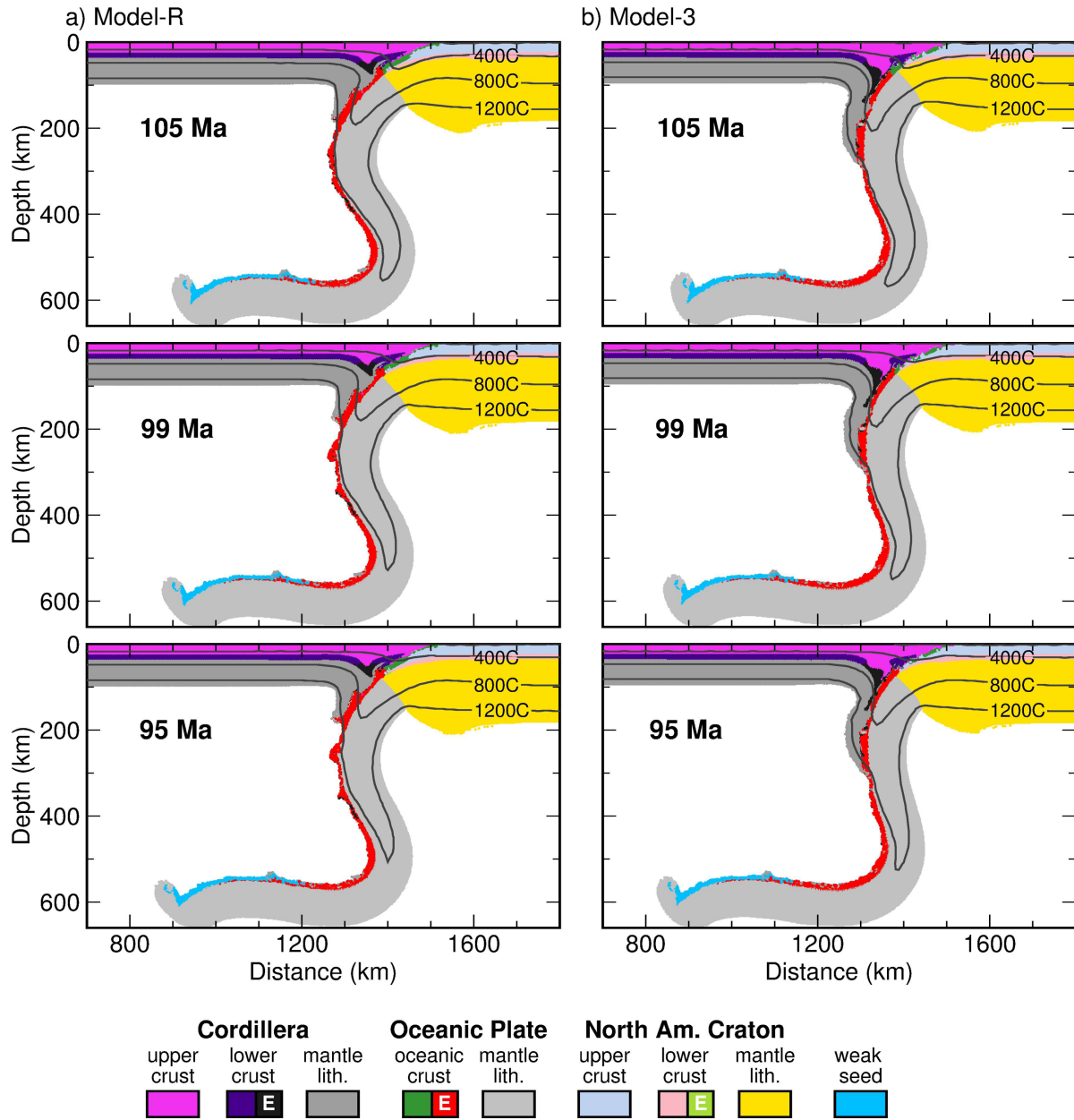
Figure 3.7. Densification effect on slab breakoff. a) Model-R with continental lower crust densification. Slab breakoff does not occur. b) Model-3 with no continental lower crust densification. Slab breakoff does not occur. E= eclogite in the legend.

b) Cratonic mantle lithosphere density

We now examine the role of the lithospheric mantle of cratonic North America by varying

its density. We compare Model-1 and Model-4 relative to the reference model by changing the

oceanic mantle lithosphere strength to f=1 and varying the density of the cratonic lithospheric mantle between Model-1 (3250 kg/m^3) and Model-4 (3210 kg/m^3) at the same temperature (Table 3.2).

Unlike the Model-R, in which the subducted slab remains attached to the cratonic North America lithosphere, Models 1 and 4, both of which are characterized by a low strength oceanic lithospheric mantle, exhibit slab breakoff. Both models shown necking of the slab beginning at 105 Ma (5 Myrs after collision). In Model-4, slab breakoff occurs later and at a slightly shallower depth (260 km) compared to Model-1 (~280 km). The effects of variation in the density of cratonic lithospheric mantle between Models 1 and 4 are minimal.

Varying the density of the continental lower crust (for example, due to eclogitization) seems to have little effect on the fate of the slab. However, the density of the cratonic mantle lithosphere does affect the dynamics of the slab following collision; as might be expected, a lower density, more buoyant continental lithosphere, causes the slab breakoff to occur at a shallower depth when coupled with a low strength oceanic mantle lithosphere strength.
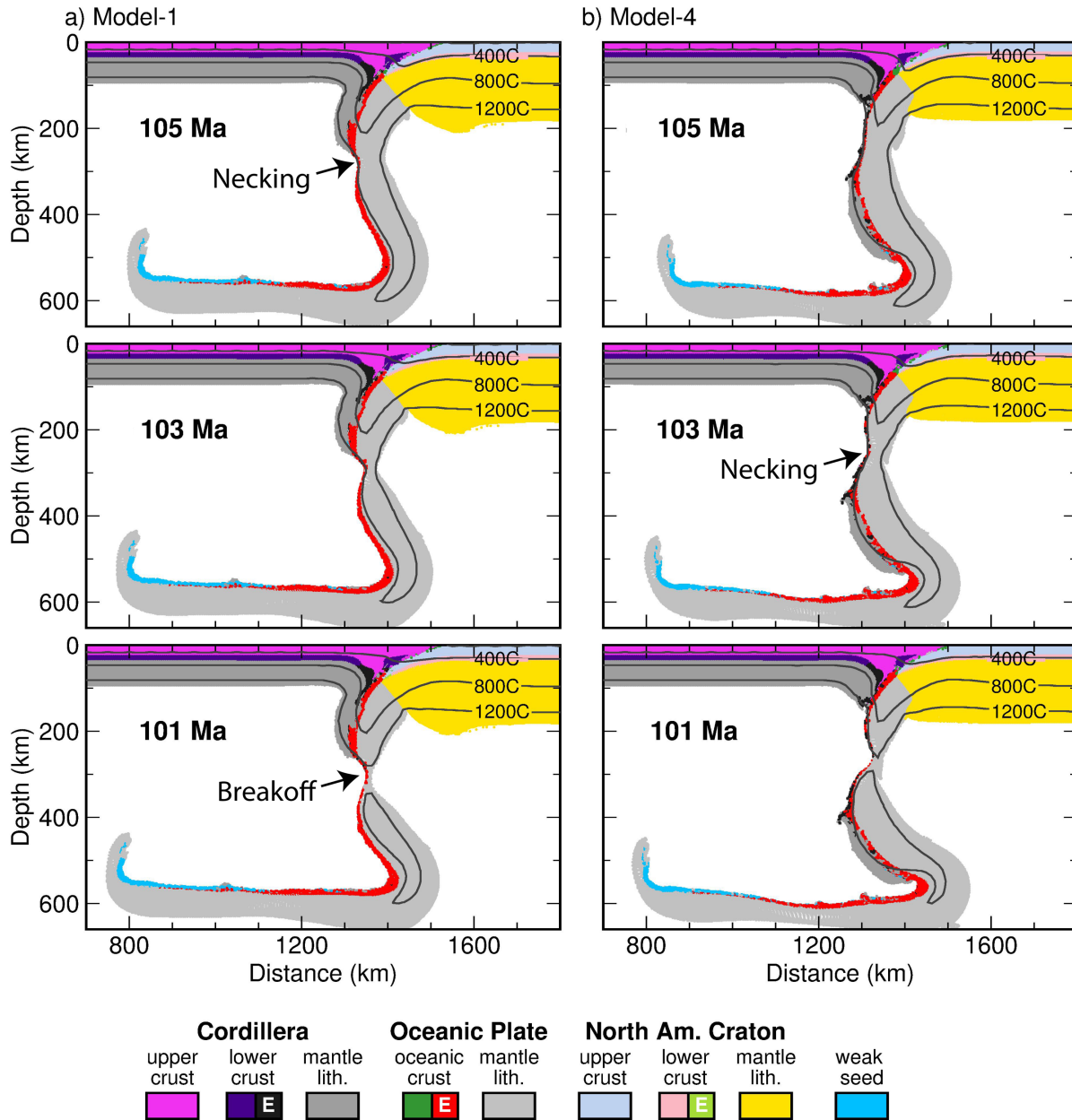
Figure 3.8. Cratonic mantle lithosphere (ML) density comparison. a) Model-1, Cratonic ML density is 3250 kg/m^3. b) Model-4, Cratonic ML density is 3210 kg/m^3. E=eclogite in the legend.

3.3.4 Convergence rate

In the final tests, we examine the effect of convergence rate in Phase 3. We first weaken the oceanic mantle lithosphere to f=1 and then compare rates of 10 (Model-1) and 5 (Model-5) cm/yr (Fig. 3.3). A width of 500 km of oceanic lithosphere is subducted, bringing the cratonic

North American lithosphere into the subduction zone, followed by a further 300 km of convergence. In the reference model, 15 Myrs subduction (from 125 to 110 Ma in geological time) at 10 cm/yr preceded collision. We now test a convergence rate of 5 cm/yr from the start of Phase 3 of the models. This implies that subduction began at 130 Ma, in order to subduct the same length of oceanic lithosphere, resulting in collision at 110 Ma.

Fig. 3.9a (Model-1) indicates that the slab starts to neck at 105 Ma and break off at ~101 Ma (9 Myrs after collision) and at a depth of ~280 km. In Model-5, slab necking begins at 106 Ma followed by breakoff at 104 Ma (6 Myrs after collision) and at a shallower depth (~ 260 km) than Model-1. Model-5 is also characterized by a shallower slab dip during subduction, a more extended (longer) detached slab, and a shorter interval between collision and breakoff.
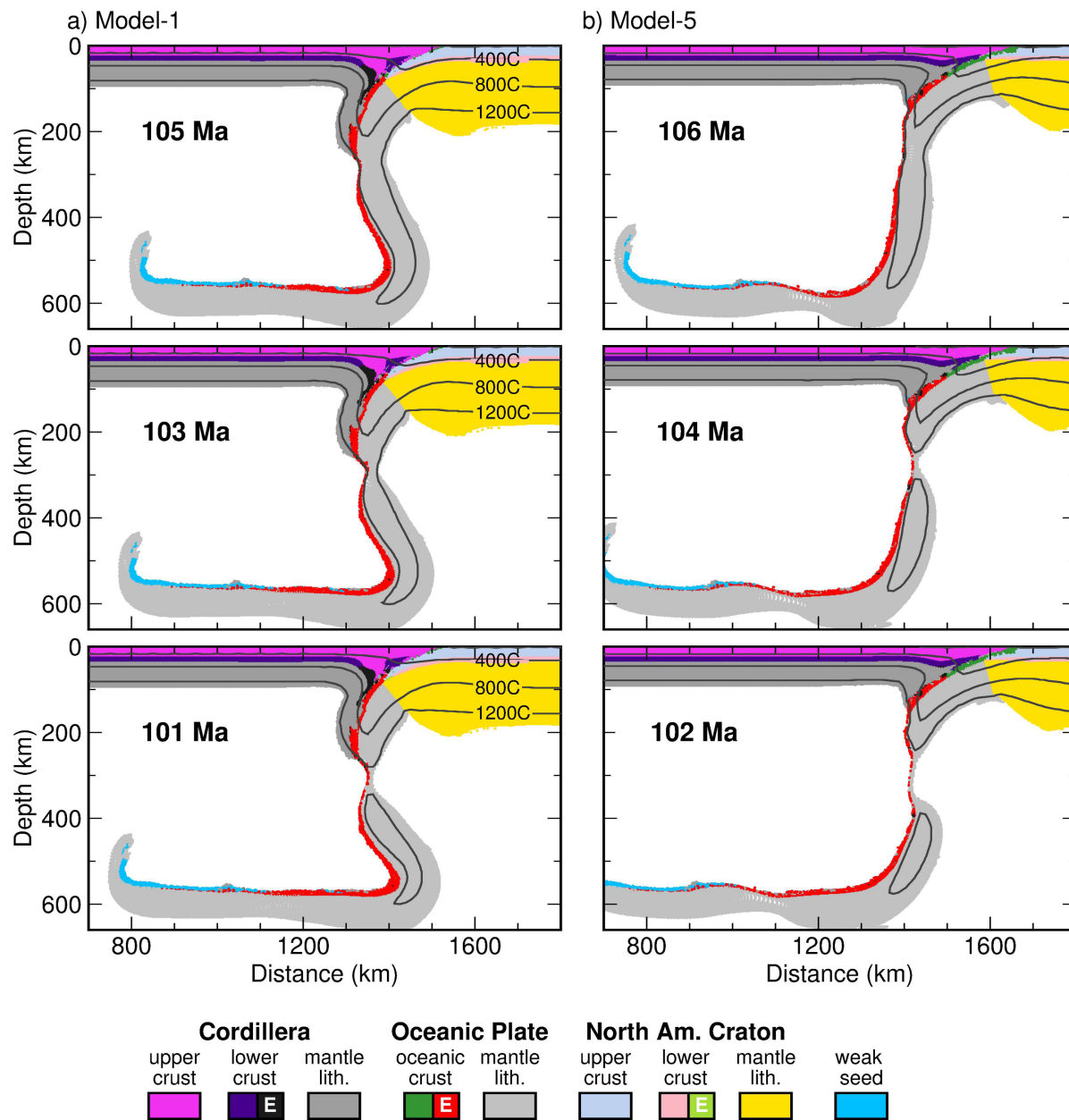
Figure 3.9. Convergence effect on the slab breakoff. a) Model-1, convergence rate = 10 cm/yr. b) Model-5, convergence rate = 5 cm/yr. E=eclogitization in the legend.

3.4 Discussion

The goal of this paper is to test, by implementing numerical geodynamic models, aspects of the collisional (west-dipping subduction) model of the Cordilleran orogeny. To assess the implication of our models, we first outline some of the main characteristics of the collisional

model and the available geological constraints. We then determine our preferred geodynamic model and discuss its implications (e.g. topography) for the collisional model of Cordillera. We end by assessing the limitations of our results.

3.4.1 Characteristics of the collisional model

Collisional models of the Cordillera involving west-dipping subduction, despite variations in the inferred timing, suture locations and nature of the upper Cordilleran plate (Johnston and Borel, 2007; Johnston, 2008; Hildebrand, 2009; Sigloch and Mihalynuk, 2013), are all broadly similar. We utilize the model of Johnston (2008) and here summarize its main features and the geological observations on which it is based. Initiation of subduction of North American oceanic lithosphere beneath the Cordillera at ~120 Ma explains the Omineca Magmatic Belt (OMB) intrusions of the eastern Cordillera as a magmatic arc (Fig. 3.1) (Hart et al., 2004; Johnston, 2008). A change in the OMB magmatism from oxidized, magnetite-bearing, I-type plutons to reduced, ilmenite-bearing, S-type plutons at ~110 Ma (Hart et al., 2004) is inferred to record entry of the North American continental margin into the trench initiating Cordilleran – North American collision. A cryptic suture (Fig. 3.1), along or east of the OMB is implicit in this collisional model. The only exposed ophiolitic surface trace of the suture may be the Cretaceous Salmon River ophiolite, Idaho. There is no geophysical evidence to suggest the presence of a subducted oceanic slab attached to and dangling beneath the eastern Cordilleran orogeny (Bao et al., 2014; Chen et al., 2018) implying that the subducting slab detached (breakoff) from the North American continental lithosphere sometime during or after collision. The 92 - 95 Ma alkalic and locally silica-undersaturated gabbros of the Tombstone suite may represent a magmatic record of slab break-off, implying that detachment and sinking of the subducted slab occurred some 15 to 18 Myrs after collision (Hildebrand and Whalen, 2017).

3.4.2 Preferred model

Here, we identify our preferred geodynamic model based on comparison against the geological constraints. Our models demonstrate that continental and oceanic mantle lithosphere strengths are key controls on the fate of the subducted slab. In contrast, changes in the density structure and convergence rate have little effect. In our preferred model (Fig. 3.10), the most significant observation is the sharp, steeply-dipping contact between the Cordillera and the North American continent after slab detachment, consistent with recent geophysical observations (Chen et al.; Bao et al., 2014). In terms of convergence rate, our models (Fig. 3.9) show that lower convergence rates result in a reduction in the interval between collision and slab breakoff.

Given these considerations, our preferred model is Model-P. The parameters that yield the best fit to the geological constraints include continental mantle lithosphere strength of f=2.5 and oceanic mantle lithosphere strength of f=5; a convergence rate of 5 cm/yr, and eclogitization for lower crusts. We utilize a density of 3250 kg/m^3 for the cratonic lithospheric mantle. The preferred model results in slab necking at 97 Ma and breakoff at ~95 Ma. Continental dripping occurs at a distance of ~400-1000 km distance east of the trench (Fig. 3.10) as the model proceeds, probably reflecting mantle (convective) erosion.
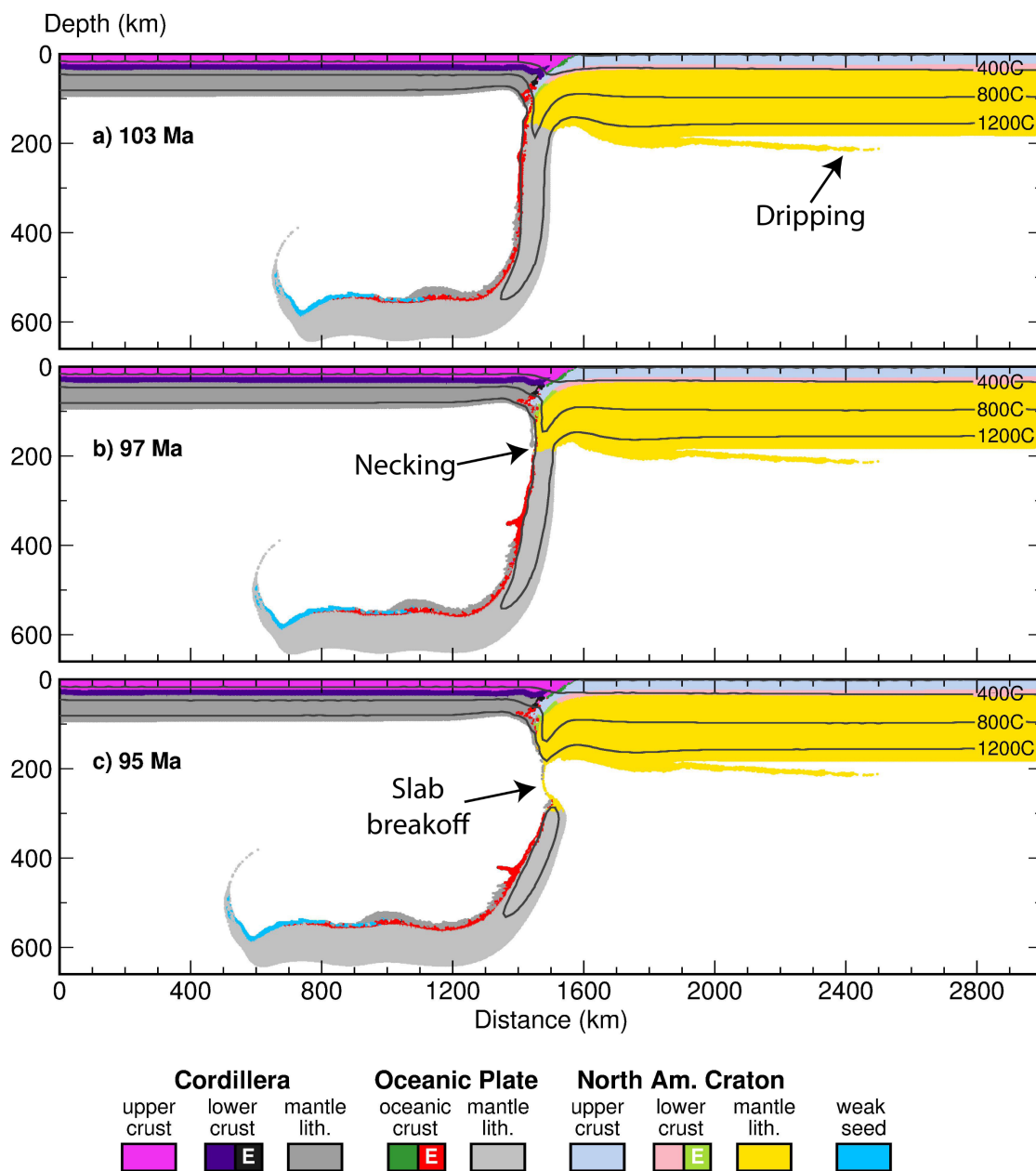
Figure 3.10. Preferred model between 103 and 95 Ma. Model parameters are in Table 3.2.

3.4.3 Resulting topography and subsidence

Our model makes predictions regarding the topographic evolution of the upper

Cordilleran and lower North American plates during and after collision. Based on our preferred

model (Fig. 3.10), we examine the topographic evolution of the orogen (Fig. 3.11) after

continental collision. We record the topographic evolution from 104 Ma, the time of cessation of

convergence (6 Myr after collision) to 95 Ma, 1 Myr after slab breakoff. The topography at 104

Ma shows two peaks (Fig. 3.11) including a 1-km elevation high culmination (all elevations are

given relative to the reference level, 0 km in the model) located 200 km west of the trench (all

distances are given relative to the trench), and a 2-km high culmination 200 km further east

(immediately over the suture). Between 104 Ma and slab break-off at 96 Ma, the more westerly

culmination migrates slowly (~12.5 km/a) to the east and increases in amplitude. Until at 96 Ma,

it is located 100 km west of the original suture. Above slab breakoff, the culmination's elevation

climbs to 3 km. Conversely, the culmination (highest elevation at 104 Ma) originally located

over the suture remains relatively fixed in location but steadily diminishes in height and passing

below sea level at 100 Ma. Upon slab breakoff, the elevation of the site of the suture has been

dragged down to ~1 km below sea level. Our estimated maximum elevation (the 3 km high

culmination located 100 km west of the suture) is consistent with previous estimates of

Cretaceous topographic relief (Chase et al., 1998) and matches previous studies showing that

slab breakoff leads to uplift (Buiter et al., 2002; Duretz et al., 2011) due to the rebound of the

lower plate combined with asthenospheric upwelling (Bottrill et al., 2012; Magni et al., 2017).
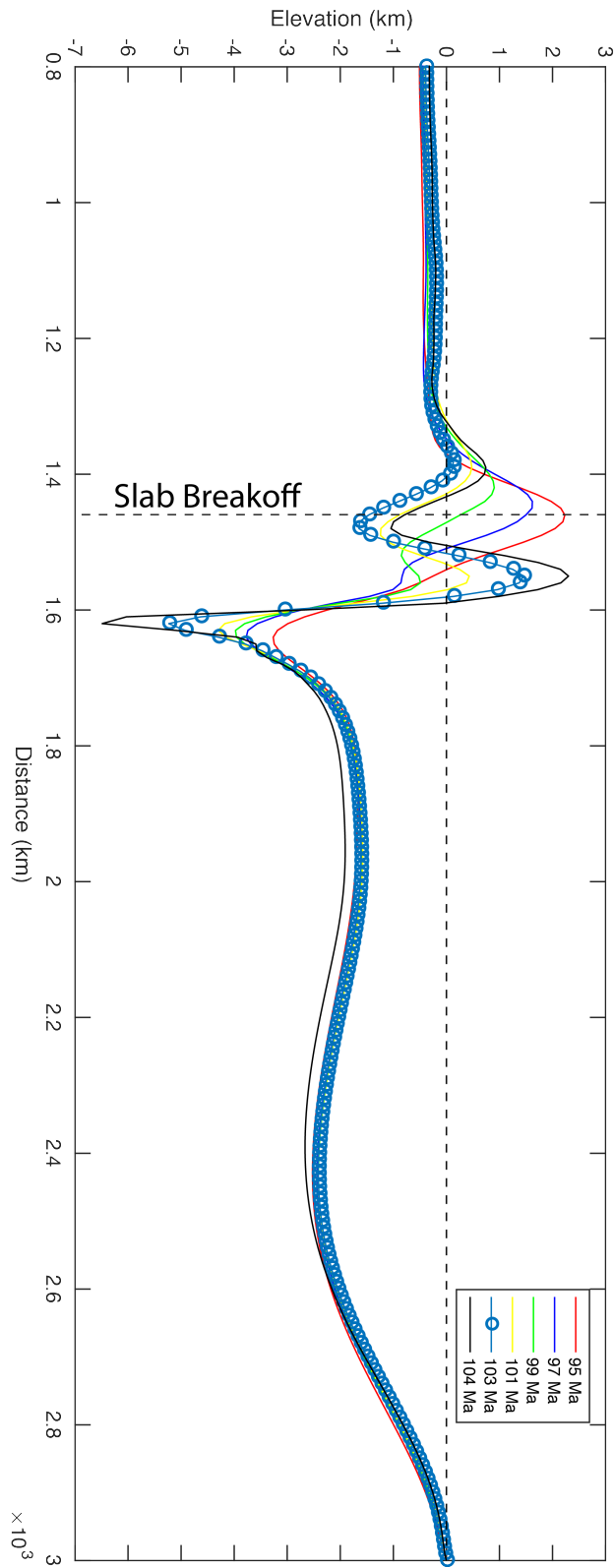
Figure 3.11. Topography plots since 104 to 95 Ma referred to preferred model. Horizontal distance is cropped between 1000 to 3000 km (no significant deformation between 0-1000 km).

East of the cryptic suture, the North American craton subsides (Fig. 3.11). Significant cratonic subsidence extends >1000 km east of the suture, with ~ 4 km of subsidence adjacent to the boundary with the Cordilleran upper plate (Fig. 3.11). Our predicted topography closely resembles, in magnitude and extent, the known topographic features of the Cordillera including the Cordilleran foreland basin. Our results suggest that collision in response to west-dipping subduction can explain Cordilleran topographic evolution including the generation of elevations of 3 km and the development of a foreland basin.

3.4.4 Limitations of our results

Our models have limitations that should be considered. Our focus was on the upper mantle slab dynamics, and the descending slabs were prohibited from penetrating the transition boundary at 660 km. This may affect the subduction process. Our model domain is expressed in 2D, and lacks the ability to implement lateral (perpendicular to the 2D plane) dynamics. Finally, our modeling does not take into account the post-95 Ma evolution of the Cordillera. Significant events, including Laramide orogeny and the development of the Rocky Mountain fold and thrust belt entirely post-date the processes investigated here.

3.5 Conclusion

We have demonstrated that a collisional model of Cordilleran evolution involving west-dipping subduction of North American oceanic lithosphere beneath the east margin of the Cordillera can successfully be geodynamically modelled using reasonable parameters. The parameters employed in our preferred model include: with continental lithospheric mantle strength f=2.5, oceanic lithospheric mantle strength f=5, and convergence rate of 5 cm/yr. Our geodynamic models show that 1) the strength of the lithospheric mantle has a significant effect on the subduction processes; 2) convergence rate noticeably affects the fate of the subducting

slab; and 3) the density of the continental lithospheric mantle and the lower continental crust have little effect on the fate of the subducting slab.

We demonstrated that collision and slab breakoff may lead to significant changes in surface topography. The elevation high culmination changes from 1 km, prior to the slab breakoff, to 3 km, after slab breakoff. We also depicted that the west-dipping model build a foreland geometry extends >1000 km east of the suture, with ~ 4 km of subsidence adjacent to the boundary with the Cordilleran upper plate.

3.6 References

Ault, A.K., Flowers, R.M., and Bowring, S.A., 2015, Synchroneity of cratonic burial phases and gaps in the kimberlite record: Episodic magmatism or preservational bias? Earth and Planetary Science Letters, v. 410, p. 97–104, doi:10.1016/j.epsl.2014.11.017.

Bao, X., Eaton, D.W., and Guest, B., 2014, Plateau uplift in western Canada caused by lithospheric delamination along a craton edge: Nature Geoscience, v. 7, p. 830–833, doi:10.1038/ngeo2270.

Beaumont, C., 1981, Foreland basins: Geophysical Journal International, v. 65, p. 291–329, doi:10.1111/j.1365-246X.1981.tb02715.x.

Beaumont, C., Nguyen, M.H., Jamieson, R.A., and Ellis, S., 2006, Crustal flow modes in large hot orogens: Geological Society, London, Special Publications, v. 268, p. 91–145, doi:10.1144/GSL.SP.2006.268.01.05.

Bottrill, A.D., van Hunen, J., and Allen, M.B., 2012, Insight into collision zone dynamics from topography: numerical modelling results and observations: Solid Earth, v. 3, p. 387–399, doi:10.5194/se-3-387-2012.

Buiter, S.J.H., Govers, R., and Wortel, M.J.R., 2002, Two-dimensional simulations of surface deformation caused by slab detachment: Tectonophysics, v. 354, p. 195–210, doi:10.1016/S0040-1951(02)00336-0.

Burov, E.B., and Diament, M., 1995, The effective elastic thickness (Te) of continental lithosphere: What does it really mean? Journal of Geophysical Research: Solid Earth, v. 100, p. 3905–3927, doi:10.1029/94JB02770.

Chase, C.G., Gregory-Wodzicki, K.M., Parrish, J., and Decelles, P.G., 1998, Topographic history of the Western Cordillera of North America and Controls on Climate: Oxford University Press, https://books.google.ca/books?hl=en&lr=&id=HbamVUkDTLMC&oi=fnd&pg=PA73&dq=cordillera+cretaceous+topography&ots=qek7hkWwn_&sig=KpQLIAujA18MC7z9IsgYEZ1_f4I#v=onepage&q=cordillera%20cretaceous%20topography&f=false (accessed October 2018).

Chen, Y., Gu, Y.J., and Hung, S.-H., 2018, A New Appraisal of Lithospheric Structures of the Cordillera-Craton Boundary Region in Western Canada: Tectonics, v. 37, p. 3207–3228, doi:10.1029/2018TC004956.

Chen, Y., Gu, Y.J., and Hung, S.-H. A New Appraisal of Lithospheric Structures of the Cordillera-Craton Boundary Region in Western Canada: Tectonics, v. 0, doi:10.1029/2018TC004956.

Coney, P.J., Jones, D.L., and Monger, W.H.J., 1980, Cordilleran suspect terranes: Nature, v. 288, p. 329–333.

Currie, C.A., and Beaumont, C., 2011, Are diamond-bearing Cretaceous kimberlites related to low-angle subduction beneath western North America? Earth and Planetary Science Letters, v. 303, p. 59–70, doi:10.1016/j.epsl.2010.12.036.

DeCelles, P.G., 2004, Late Jurassic to Eocene evolution of the Cordilleran thrust belt and foreland basin system, western U.S.A.: American Journal of Science, v. 304, p. 105–168, doi:10.2475/ajs.304.2.105.

DeCelles, P.G., Ducea, M.N., Kapp, P., and Zandt, G., 2009, Cyclicity in Cordilleran orogenic systems: Nature Geoscience, v. 2, p. 251–257, doi:10.1038/ngeo469.

Ducea, M., 2001, The California Arc: Thick Granitic Batholiths, Eclogitic Residues,
Lithospheric-Scale Thrusting, and Magmatic Flare-Ups: GSA TODAY, p. 7.

Duretz, T., Gerya, T.V., and May, D.A., 2011, Numerical modelling of spontaneous slab
breakoff and subsequent topographic response: Tectonophysics, v. 502, p. 244–256,
doi:10.1016/j.tecto.2010.05.024.

Flück, P., Hyndman, R.D., and Lowe, C., 2003, Effective elastic thickness Te of the lithosphere
in western Canada: Journal of Geophysical Research: Solid Earth, v. 108,
doi:10.1029/2002JB002201.

Fullsack, P., 1995, An arbitrary Lagrangian-Eulerian formulation for creeping flows and its
application in tectonic models: Geophysical Journal International, v. 120, p. 1–23,
doi:10.1111/j.1365-246X.1995.tb05908.x.

Gleason, G.C., and Tullis, J., 1995, A flow law for dislocation creep of quartz aggregates
determined with the molten salt cell: Tectonophysics, v. 247, p. 1–23, doi:10.1016/0040-
1951(95)00011-B.

Gordey, S.P., and Anderson, R.G., 1993, Evolution of the Northern Cordilleran Miogeocline,
Nahanni map area (105I), Yukon and Northwest Territories: Ottawa, Minister of Supply
and Services Canada, Memoir / Geological Survey of Canada 428, 214 p.

Griffin, W.L., Pearson, N.J., Belousova, E., Jackson, S.E., van Achterbergh, E., O'Reilly, S.Y.,
and Shee, S.R., 2000, The Hf isotope composition of cratonic mantle: LAM-MC-ICPMS
analysis of zircon megacrysts in kimberlites: Geochimica et Cosmochimica Acta, v. 64,
p. 133–147, doi:10.1016/S0016-7037(99)00343-9.

Gunn, R., 1949, Isostasy extended: J. Geol., v. 57, p. 263–279.

Harris, M.J., Symons, D.T.A., Blackburn, W.H., and Hart, C.J.R., 1999, Paleomagnetic and
geobarometric study of the Late Cretaceous Mount Lorne stock, southern Yukon
Territory: v. 36, p. 11.

Hart, C.J.R., Goldfarb, R.J., Lewis, L.L., and Mair, J.L., 2004, The Northern Cordilleran Mid-Cretaceous Plutonic Province: Ilmenite/Magnetite-series Granitoids and Intrusion-related Mineralisation: Resource Geology, v. 54, p. 253–280, doi:10.1111/j.1751-3928.2004.tb00206.x.

Heaman, L.M., Kjarsgaard, B.A., and Creaser, R.A., 2004, The temporal evolution of North American kimberlites: Lithos, v. 76, p. 377–397, doi:10.1016/j.lithos.2004.03.047.

Heaman, L., kjarsgaard, B., and Creaser, R., 2003, The timing of kimberlite magmatism in North America: implications for global kimberlite genesis and diamond exploration: Lithos, v. 71, p. 153–184, doi:10.1016/j.lithos.2003.07.005.

Hildebrand, R.S., 2009, Did Westward Subduction Cause Cretaceous–Tertiary Orogeny in the North American Cordillera?, *in* Geological Society of America Special Papers, Geological Society of America, v. 457, p. 1–71, doi:10.1130/2009.2457.

Hildebrand, R.S., 2014, Geology, Mantle Tomography, and Inclination Corrected Paleogeographic Trajectories Support Westward Subduction During Cretaceous Orogenesis in the North American Cordillera: Geoscience Canada, v. 41, p. 207, doi:10.12789/geocanj.2014.41.032.

Hildebrand, R.S., and Whalen, J.B., 2017, The Tectonic Setting and Origin of Cretaceous Batholiths within the North American Cordillera: The Case for Slab Failure Magmatism and Its Significance for Crustal Growth: Geological Society of America, 123 p.

Hirano, N., 2011, Petit-spot volcanism: A new type of volcanic zone discovered near a trench: GEOCHEMICAL JOURNAL, v. 45, p. 157–167, doi:10.2343/geochemj.1.0111.

Hirano, N. et al., 2006, Volcanism in Response to Plate Flexure: Science, v. 313, p. 1426–1428, doi:10.1126/science.1128235.

Hyndman, R.D., and Currie, C.A., 2011, Why is the North America Cordillera high? Hot backarcs, thermal isostasy, and mountain belts: Geology, v. 39, p. 783–786, doi:10.1130/G31998.1.

Hyndman, R.D., Currie, C.A., Mazzotti, S., and Frederiksen, A., 2009, Temperature control of continental lithosphere elastic thickness, Te vs Vs: Earth and Planetary Science Letters, v. 277, p. 539–548, doi:10.1016/j.epsl.2008.11.023.

Ito, E., and Katsura, T., 1989, A temperature profile of the mantle transition zone: Geophysical Research Letters, v. 16, p. 425–428, doi:10.1029/GL016i005p00425.

Johnson, R.B., and DeGraff, J.V., 1988, Principle of Engineering Geology: Wiley, 512 p.

Johnston, S.T., 2008, The Cordilleran Ribbon Continent of North America: Annual Review of Earth and Planetary Sciences, v. 36, p. 495–530, doi:10.1146/annurev.earth.36.031207.124331.

Johnston, S.T., and Borel, G.D., 2007, The odyssey of the Cache Creek terrane, Canadian Cordillera: Implications for accretionary orogens, tectonic setting of Panthalassa, the Pacific superwell, and break-up of Pangea: Earth and Planetary Science Letters, v. 253, p. 415–428, doi:10.1016/j.epsl.2006.11.002.

Karato, S. -i., and Wu, P., 1993, Rheology of the Upper Mantle: A Synthesis: Science, v. 260, p. 771–778, doi:10.1126/science.260.5109.771.

Kjarsgaard, B.A., Heaman, L.M., Sarkar, C., and Pearson, D.G., 2017, The North America mid-Cretaceous kimberlite corridor: Wet, edge-driven decompression melting of an OIB-type deep mantle source: Geochemistry, Geophysics, Geosystems, v. 18, p. 2727–2747, doi:10.1002/2016GC006761.

Levitt, D.A., and Sandwell, D.T., 1995, Lithospheric bending at subduction zones based on depth soundings and satellite gravity: Journal of Geophysical Research: Solid Earth, v. 100, p. 379–400, doi:10.1029/94JB02468.

Liu, L., 2014, Constraining Cretaceous subduction polarity in eastern Pacific from seismic tomography and geodynamic modeling: Constrain Cretaceous subduction polarity: Geophysical Research Letters, v. 41, p. 8029–8036, doi:10.1002/2014GL061988.

Liu, S., and Currie, C.A., 2016, Farallon plate dynamics prior to the Laramide orogeny: Numerical models of flat subduction: Tectonophysics, v. 666, p. 33–47, doi:10.1016/j.tecto.2015.10.010.

Machida, S., Kogiso, T., and Hirano, N., 2017, Petit-spot as definitive evidence for partial melting in the asthenosphere caused by CO2: Nature Communications, v. 8, p. 14302, doi:10.1038/ncomms14302.

Mackwell, S.J., Zimmerman, M.E., and Kohlstedt, D.L., 1998, High-temperature deformation of dry diabase with application to tectonics on Venus: Journal of Geophysical Research: Solid Earth, v. 103, p. 975–984, doi:10.1029/97JB02671.

Magni, V., Allen, M.B., van Hunen, J., and Bouilhol, P., 2017, Continental underplating after slab break-off: Earth and Planetary Science Letters, v. 474, p. 59–67, doi:10.1016/j.epsl.2017.06.017.

McCandless, T.E., 1999, Kimberlites: Mantle Expressions of Deep-Seated Subduction: , p. 5.

McCausland, P.J.A., Symons, D.T.A., Hart, C., and Blackburn, W.H., 2006, Assembly of the northern Cordillera: New paleomagnetic evidence for coherent, moderate Jurassic to Eocene motion of the Intermontane belt and Yukon-Tananaterranes: v. 46, 147 p.

Monger, J.W.H., Price, R.A., and Tempelman-Kluit, D.J., 1982, Tectonic accretion and the origin of the two major metamorphic and plutonic welts in the Canadian Cordillera: Geology, v. 10, p. 70, doi:10.1130/0091-7613(1982)10<70:TAATOO>2.0.CO;2.

Oldow, J.S., Bally, A.W., and Avé Lallemant, H.G., 1990, Transpression, orogenic float, and lithospheric balance: Geology, v. 18, p. 991, doi:10.1130/0091-7613(1990)018<0991:TOFALB>2.3.CO;2.

Painter, C.S., and Carrapa, B., 2013, Flexural versus dynamic processes of subsidence in the North American Cordillera foreland basin: Geophysical Research Letters, v. 40, p. 4249–4253, doi:10.1002/grl.50831.

Pilet, S., Abe, N., Rochat, L., Kaczmarek, M.-A., Hirano, N., Machida, S., Buchs, D.M., Baumgartner, P.O., and Müntener, O., 2016, Pre-subduction metasomatic enrichment of the oceanic lithosphere induced by plate flexure: Nature Geoscience, v. 9, p. 898–903, doi:10.1038/ngeo2825.

Price, R.A., 1981, The Cordilleran foreland thrust and fold belt in the southern Canadian Rocky Mountains: Geological Society, London, Special Publications, v. 9, p. 427–448, doi:10.1144/GSL.SP.1981.009.01.39.

Pysklywec, R.N., and Beaumont, C., 2004, Intraplate tectonics: feedback between radioactive thermal weakening and crustal deformation driven by mantle lithosphere instabilities: Earth and Planetary Science Letters, v. 221, p. 275–292, doi:10.1016/S0012-821X(04)00098-6.

le Roex, A.P., 1986, Geochemical correlation between southern African kimberlites and South Atlantic hotspots: Nature, v. 324, p. 243–245.

Sato, Y., Hirano, N., Machida, S., Yamamoto, J., Nakanishi, M., Ishii, T., Taki, A., Yasukawa, K., and Kato, Y., 2018, Direct ascent to the surface of asthenospheric magma in a region of convex lithospheric flexure: International Geology Review, v. 60, p. 1231–1243, doi:10.1080/00206814.2017.1379912.

Sharp, W.E., 1974, A plate tectonic origin for diamond-bearing kimberlites: Earth and Planetary Science Letters, v. 21, p. 351–354, doi:10.1016/0012-821X(74)90173-3.

Sigloch, K., and Mihalynuk, M.G., 2013, Intra-oceanic subduction shaped the assembly of Cordilleran North America: Nature, v. 496, p. 50–56, doi:10.1038/nature12019.

Sigloch, K., and Mihalynuk, M.G., 2017, Mantle and geological evidence for a Late Jurassic−Cretaceous suture spanning North America: GSA Bulletin, doi:10.1130/B31529.1.

Syracuse, E.M., van Keken, P.E., and Abers, G.A., 2010, The global range of subduction zone thermal models: Physics of the Earth and Planetary Interiors, v. 183, p. 73–90, doi:10.1016/j.pepi.2010.02.004.

Timoshenko, S., and MacCullough, G.H., 1935, Elements of Strength of Materials: D. Van Nostrand Company, Inc.

Torsvik, T.H., Steinberger, B., Ashwal, L.D., Doubrovine, P.V., and Trønnes, R.G., 2016, Earth evolution and dynamics—a tribute to Kevin Burke (A. Polat, Ed.): Canadian Journal of Earth Sciences, v. 53, p. 1073–1087, doi:10.1139/cjes-2015-0228.

Turcotte, D.L., and Schubert, G., 2002, Geodynamics: Cambridge University Press, 828 p.

Warren, C.J., Beaumont, C., and Jamieson, R.A., 2008, Formation and exhumation of ultra-high-pressure rocks during continental collision: Role of detachment in the subduction channel: Geochemistry, Geophysics, Geosystems, v. 9, doi:10.1029/2007GC001839.

Watts, A.B., 2001, Isostasy and flexure of the lithosphere: Cambridge ; New York, Cambridge University Press, 105–110 p.

Wyllie, P.J., 1980, The origin of kimberlite: Journal of Geophysical Research, v. 85, p. 6902, doi:10.1029/JB085iB12p06902.

Chapter 4. Conclusions and future work

Our studies provided two main tests of the collisional model of the Cordillera. First, we examined the temporal and spatial correlation between the Cordilleran OMB and the cratonic CCKC (Chapter 2). We used the Petit-spot volcanoes that characterize the subducting Pacific plate as a modern analogue. It has been suggested that these small alkali basaltic submarine volcanoes are produced by tensile stress that develops due to flexure of the subducting Pacific plate into the forebulge located oceanward of the trench. We tested this model and demonstrated that it was a viable explanation of Petit-spot magmatism. We then applied this model to continental North America. Our calculations show that the CCKC could be explained by the same process during attempted subduction of the North American continent to the west beneath the Cordillera. In our model, the coeval OMB and CCKC are upper and lower plate manifestations of subduction: the OMB represents the arc, and the CCKC is the result of flexure of the lower plate as it bends into the trench separating the two.

Based on this Cordillera-Craton geological application, we further investigated the fate of the oceanic slab that is hypothesized to have separated the Cordilleran and North American continental domains (Chapter 3). We geodynamically modelled the Cordilleran collision involving west-dipping subduction using reasonable parameters. The parameters employed in our preferred model include: with continental lithospheric mantle strength f=2.5, oceanic lithospheric mantle strength f=5, and convergence rate of 5 cm/yr. Our geodynamic models show that 1) the strength of the lithospheric mantle has a significant effect on the subduction processes; 2) convergence rate noticeably affects the fate of the subducting slab; 3) the density of the continental lithospheric mantle and the lower continental crust have little effect on the fate of the subducting slab. Our

model explained available geological observations, including providing a reasonable prediction of the post-collisional topographic evolution of the orogen and its immediate foreland.

4.1 Future work

Some future works should be addressed based upon our studies. First, our geodynamic modelling yielded slab break-off at about 95 Ma, consistent with previous interpretations of the Tombstone Suite plutons as being a magmatic record of slab break-off. However, this is an empirical finding and lacks petrological support. Therefore, we suggest examining the P-T evolution in our models to predict the timing, location and nature of magmatism during and after collision.

Second, in our geodynamic model, we extrapolate our model to 660 km from the surface to investigate the fate of the subducting slab. However, the mantle extends a depth of 2900 km from the surface. Sigloch and Mihalynuk (2013, 2017) have interpreted slab walls tomographically imaged beneath eastern North America as the remnants of the North American oceanic lithosphere subducted westward beneath the Cordillera. In order to test this interpretation and to understand slab behaviour in the lower mantle, our models need to be expanded to cover the entire mantle.

In Chapter 2, we focused on the elastic property of the North American craton. In Chapter 3, our model was implemented utilizing viscous-plastic materials. Hence our two studies employed two distinct types of the strength properties in modeling the North American craton. I suggest that future studies include a comprehensive strength yield analysis in order to test for compatibility of viscous-plastic and elastic models.

References

Ault, A.K., Flowers, R.M., and Bowring, S.A., 2015, Synchroneity of cratonic burial phases and gaps in the kimberlite record: Episodic magmatism or preservational bias? Earth and Planetary Science Letters, v. 410, p. 97–104, doi:10.1016/j.epsl.2014.11.017.

Bao, X., Eaton, D.W., and Guest, B., 2014, Plateau uplift in western Canada caused by lithospheric delamination along a craton edge: Nature Geoscience, v. 7, p. 830–833, doi:10.1038/ngeo2270.

Beaumont, C., 1981, Foreland basins: Geophysical Journal International, v. 65, p. 291–329, doi:10.1111/j.1365-246X.1981.tb02715.x.

Beaumont, C., Nguyen, M.H., Jamieson, R.A., and Ellis, S., 2006, Crustal flow modes in large hot orogens: Geological Society, London, Special Publications, v. 268, p. 91–145, doi:10.1144/GSL.SP.2006.268.01.05.

Bottrill, A.D., van Hunen, J., and Allen, M.B., 2012, Insight into collision zone dynamics from topography: numerical modelling results and observations: Solid Earth, v. 3, p. 387–399, doi:10.5194/se-3-387-2012.

Buiter, S.J.H., Govers, R., and Wortel, M.J.R., 2002, Two-dimensional simulations of surface deformation caused by slab detachment: Tectonophysics, v. 354, p. 195–210, doi:10.1016/S0040-1951(02)00336-0.

Burov, E.B., and Diament, M., 1995, The effective elastic thickness (Te) of continental lithosphere: What does it really mean? Journal of Geophysical Research: Solid Earth, v. 100, p. 3905–3927, doi:10.1029/94JB02770.

Chase, C.G., Gregory-Wodzicki, K.M., Parrish, J., and Decelles, P.G., 1998, Topographic history of the Western Cordillera of North America and Controls on Climate: Oxford University Press, https://books.google.ca/books?hl=en&lr=&id=HbamVUkDTLMC&oi=fnd&pg=PA73&dq=cordillera+cretaceous+topography&ots=qek7hkWwn_&sig=KpQLIAujA18MC7z9Isg

YEZ1_f4I#v=onepage&q=cordillera%20cretaceous%20topography&f=false (accessed October 2018).

Chen, Y., Gu, Y.J., and Hung, S.-H., 2018, A New Appraisal of Lithospheric Structures of the Cordillera-Craton Boundary Region in Western Canada: Tectonics, v. 37, p. 3207–3228, doi:10.1029/2018TC004956.

Chen, Y., Gu, Y.J., and Hung, S.-H. A New Appraisal of Lithospheric Structures of the Cordillera-Craton Boundary Region in Western Canada: Tectonics, v. 0, doi:10.1029/2018TC004956.

Coney, P.J., Jones, D.L., and Monger, W.H.J., 1980, Cordilleran suspect terranes: Nature, v. 288, p. 329–333.

Currie, C.A., and Beaumont, C., 2011, Are diamond-bearing Cretaceous kimberlites related to low-angle subduction beneath western North America? Earth and Planetary Science Letters, v. 303, p. 59–70, doi:10.1016/j.epsl.2010.12.036.

DeCelles, P.G., 2004, Late Jurassic to Eocene evolution of the Cordilleran thrust belt and foreland basin system, western U.S.A.: American Journal of Science, v. 304, p. 105–168, doi:10.2475/ajs.304.2.105.

DeCelles, P.G., Ducea, M.N., Kapp, P., and Zandt, G., 2009, Cyclicity in Cordilleran orogenic systems: Nature Geoscience, v. 2, p. 251–257, doi:10.1038/ngeo469.

Ducea, M., 2001, The California Arc: Thick Granitic Batholiths, Eclogitic Residues, Lithospheric-Scale Thrusting, and Magmatic Flare-Ups: GSA TODAY, p. 7.

Duretz, T., Gerya, T.V., and May, D.A., 2011, Numerical modelling of spontaneous slab breakoff and subsequent topographic response: Tectonophysics, v. 502, p. 244–256, doi:10.1016/j.tecto.2010.05.024.

Flück, P., Hyndman, R.D., and Lowe, C., 2003, Effective elastic thickness Te of the lithosphere in western Canada: Journal of Geophysical Research: Solid Earth, v. 108, doi:10.1029/2002JB002201.

Fullsack, P., 1995, An arbitrary Lagrangian-Eulerian formulation for creeping flows and its application in tectonic models: Geophysical Journal International, v. 120, p. 1–23, doi:10.1111/j.1365-246X.1995.tb05908.x.

Gleason, G.C., and Tullis, J., 1995, A flow law for dislocation creep of quartz aggregates determined with the molten salt cell: Tectonophysics, v. 247, p. 1–23, doi:10.1016/0040-1951(95)00011-B.

Gordey, S.P., and Anderson, R.G., 1993, Evolution of the Northern Cordilleran Miogeocline, Nahanni map area (105I), Yukon and Northwest Territories: Ottawa, Minister of Supply and Services Canada, Memoir / Geological Survey of Canada 428, 214 p.

Griffin, W.L., Pearson, N.J., Belousova, E., Jackson, S.E., van Achterbergh, E., O'Reilly, S.Y., and Shee, S.R., 2000, The Hf isotope composition of cratonic mantle: LAM-MC-ICPMS analysis of zircon megacrysts in kimberlites: Geochimica et Cosmochimica Acta, v. 64, p. 133–147, doi:10.1016/S0016-7037(99)00343-9.

Gunn, R., 1949, Isostasy extended: J. Geol., v. 57, p. 263–279.

Harris, M.J., Symons, D.T.A., Blackburn, W.H., and Hart, C.J.R., 1999, Paleomagnetic and geobarometric study of the Late Cretaceous Mount Lorne stock, southern Yukon Territory: v. 36, p. 11.

Hart, C.J.R., Goldfarb, R.J., Lewis, L.L., and Mair, J.L., 2004, The Northern Cordilleran Mid-Cretaceous Plutonic Province: Ilmenite/Magnetite-series Granitoids and Intrusion-related Mineralisation: Resource Geology, v. 54, p. 253–280, doi:10.1111/j.1751-3928.2004.tb00206.x.

Heaman, L.M., Kjarsgaard, B.A., and Creaser, R.A., 2004, The temporal evolution of North American kimberlites: Lithos, v. 76, p. 377–397, doi:10.1016/j.lithos.2004.03.047.

Heaman, L., kjarsgaard, B., and Creaser, R., 2003, The timing of kimberlite magmatism in North America: implications for global kimberlite genesis and diamond exploration: Lithos, v. 71, p. 153–184, doi:10.1016/j.lithos.2003.07.005.

Hildebrand, R.S., 2009, Did Westward Subduction Cause Cretaceous–Tertiary Orogeny in the North American Cordillera?, *in* Geological Society of America Special Papers, Geological Society of America, v. 457, p. 1–71, doi:10.1130/2009.2457.

Hildebrand, R.S., 2014, Geology, Mantle Tomography, and Inclination Corrected Paleogeographic Trajectories Support Westward Subduction During Cretaceous Orogenesis in the North American Cordillera: Geoscience Canada, v. 41, p. 207, doi:10.12789/geocanj.2014.41.032.

Hildebrand, R.S., and Whalen, J.B., 2017, The Tectonic Setting and Origin of Cretaceous Batholiths within the North American Cordillera: The Case for Slab Failure Magmatism and Its Significance for Crustal Growth: Geological Society of America, 123 p.

Hirano, N., 2011, Petit-spot volcanism: A new type of volcanic zone discovered near a trench: GEOCHEMICAL JOURNAL, v. 45, p. 157–167, doi:10.2343/geochemj.1.0111.

Hirano, N. et al., 2006, Volcanism in Response to Plate Flexure: Science, v. 313, p. 1426–1428, doi:10.1126/science.1128235.

Hyndman, R.D., and Currie, C.A., 2011, Why is the North America Cordillera high? Hot backarcs, thermal isostasy, and mountain belts: Geology, v. 39, p. 783–786, doi:10.1130/G31998.1.

Hyndman, R.D., Currie, C.A., Mazzotti, S., and Frederiksen, A., 2009, Temperature control of continental lithosphere elastic thickness, Te vs Vs: Earth and Planetary Science Letters, v. 277, p. 539–548, doi:10.1016/j.epsl.2008.11.023.

Ito, E., and Katsura, T., 1989, A temperature profile of the mantle transition zone: Geophysical Research Letters, v. 16, p. 425–428, doi:10.1029/GL016i005p00425.

Johnson, R.B., and DeGraff, J.V., 1988, Principle of Engineering Geology: Wiley, 512 p.

Johnston, S.T., 2008, The Cordilleran Ribbon Continent of North America: Annual Review of Earth and Planetary Sciences, v. 36, p. 495–530, doi:10.1146/annurev.earth.36.031207.124331.

Johnston, S.T., and Borel, G.D., 2007, The odyssey of the Cache Creek terrane, Canadian
    Cordillera: Implications for accretionary orogens, tectonic setting of Panthalassa, the
    Pacific superwell, and break-up of Pangea: Earth and Planetary Science Letters, v. 253, p.
    415–428, doi:10.1016/j.epsl.2006.11.002.

Karato, S. -i., and Wu, P., 1993, Rheology of the Upper Mantle: A Synthesis: Science, v. 260, p.
    771–778, doi:10.1126/science.260.5109.771.

Kjarsgaard, B.A., Heaman, L.M., Sarkar, C., and Pearson, D.G., 2017, The North America mid-
    Cretaceous kimberlite corridor: Wet, edge-driven decompression melting of an OIB-type
    deep mantle source: Geochemistry, Geophysics, Geosystems, v. 18, p. 2727–2747,
    doi:10.1002/2016GC006761.

Levitt, D.A., and Sandwell, D.T., 1995, Lithospheric bending at subduction zones based on depth
    soundings and satellite gravity: Journal of Geophysical Research: Solid Earth, v. 100, p.
    379–400, doi:10.1029/94JB02468.

Liu, L., 2014, Constraining Cretaceous subduction polarity in eastern Pacific from seismic
    tomography and geodynamic modeling: Constrain Cretaceous subduction polarity:
    Geophysical Research Letters, v. 41, p. 8029–8036, doi:10.1002/2014GL061988.

Liu, S., and Currie, C.A., 2016, Farallon plate dynamics prior to the Laramide orogeny:
    Numerical models of flat subduction: Tectonophysics, v. 666, p. 33–47,
    doi:10.1016/j.tecto.2015.10.010.

Machida, S., Kogiso, T., and Hirano, N., 2017, Petit-spot as definitive evidence for partial
    melting in the asthenosphere caused by CO_2: Nature Communications, v. 8, p. 14302,
    doi:10.1038/ncomms14302.

Mackwell, S.J., Zimmerman, M.E., and Kohlstedt, D.L., 1998, High-temperature deformation of
    dry diabase with application to tectonics on Venus: Journal of Geophysical Research:
    Solid Earth, v. 103, p. 975–984, doi:10.1029/97JB02671.

Magni, V., Allen, M.B., van Hunen, J., and Bouilhol, P., 2017, Continental underplating after slab break-off: Earth and Planetary Science Letters, v. 474, p. 59–67, doi:10.1016/j.epsl.2017.06.017.

McCandless, T.E., 1999, Kimberlites: Mantle Expressions of Deep-Seated Subduction: , p. 5.

McCausland, P.J.A., Symons, D.T.A., Hart, C., and Blackburn, W.H., 2006, Assembly of the northern Cordillera: New paleomagnetic evidence for coherent, moderate Jurassic to Eocene motion of the Intermontane belt and Yukon-Tananaterranes: v. 46, 147 p.

Monger, J.W.H., Price, R.A., and Tempelman-Kluit, D.J., 1982, Tectonic accretion and the origin of the two major metamorphic and plutonic welts in the Canadian Cordillera: Geology, v. 10, p. 70, doi:10.1130/0091-7613(1982)10<70:TAATOO>2.0.CO;2.

Oldow, J.S., Bally, A.W., and Avé Lallemant, H.G., 1990, Transpression, orogenic float, and lithospheric balance: Geology, v. 18, p. 991, doi:10.1130/0091-7613(1990)018<0991:TOFALB>2.3.CO;2.

Painter, C.S., and Carrapa, B., 2013, Flexural versus dynamic processes of subsidence in the North American Cordillera foreland basin: Geophysical Research Letters, v. 40, p. 4249–4253, doi:10.1002/grl.50831.

Pilet, S., Abe, N., Rochat, L., Kaczmarek, M.-A., Hirano, N., Machida, S., Buchs, D.M., Baumgartner, P.O., and Müntener, O., 2016, Pre-subduction metasomatic enrichment of the oceanic lithosphere induced by plate flexure: Nature Geoscience, v. 9, p. 898–903, doi:10.1038/ngeo2825.

Price, R.A., 1981, The Cordilleran foreland thrust and fold belt in the southern Canadian Rocky Mountains: Geological Society, London, Special Publications, v. 9, p. 427–448, doi:10.1144/GSL.SP.1981.009.01.39.

Pysklywec, R.N., and Beaumont, C., 2004, Intraplate tectonics: feedback between radioactive thermal weakening and crustal deformation driven by mantle lithosphere instabilities: Earth and Planetary Science Letters, v. 221, p. 275–292, doi:10.1016/S0012-821X(04)00098-6.

le Roex, A.P., 1986, Geochemical correlation between southern African kimberlites and South Atlantic hotspots: Nature, v. 324, p. 243–245.

Sato, Y., Hirano, N., Machida, S., Yamamoto, J., Nakanishi, M., Ishii, T., Taki, A., Yasukawa, K., and Kato, Y., 2018, Direct ascent to the surface of asthenospheric magma in a region of convex lithospheric flexure: International Geology Review, v. 60, p. 1231–1243, doi:10.1080/00206814.2017.1379912.

Sharp, W.E., 1974, A plate tectonic origin for diamond-bearing kimberlites: Earth and Planetary Science Letters, v. 21, p. 351–354, doi:10.1016/0012-821X(74)90173-3.

Sigloch, K., and Mihalynuk, M.G., 2013, Intra-oceanic subduction shaped the assembly of Cordilleran North America: Nature, v. 496, p. 50–56, doi:10.1038/nature12019.

Sigloch, K., and Mihalynuk, M.G., 2017, Mantle and geological evidence for a Late Jurassic−Cretaceous suture spanning North America: GSA Bulletin, doi:10.1130/B31529.1.

Syracuse, E.M., van Keken, P.E., and Abers, G.A., 2010, The global range of subduction zone thermal models: Physics of the Earth and Planetary Interiors, v. 183, p. 73–90, doi:10.1016/j.pepi.2010.02.004.

Timoshenko, S., and MacCullough, G.H., 1935, Elements of Strength of Materials: D. Van Nostrand Company, Inc.

Torsvik, T.H., Steinberger, B., Ashwal, L.D., Doubrovine, P.V., and Trønnes, R.G., 2016, Earth evolution and dynamics—a tribute to Kevin Burke (A. Polat, Ed.): Canadian Journal of Earth Sciences, v. 53, p. 1073–1087, doi:10.1139/cjes-2015-0228.

Turcotte, D.L., and Schubert, G., 2002, Geodynamics: Cambridge University Press, 828 p.

Warren, C.J., Beaumont, C., and Jamieson, R.A., 2008, Formation and exhumation of ultra-high-pressure rocks during continental collision: Role of detachment in the subduction channel: Geochemistry, Geophysics, Geosystems, v. 9, p. n/a-n/a, doi:10.1029/2007GC001839.

Watts, A.B., 2001, Isostasy and flexure of the lithosphere: Cambridge ; New York, Cambridge University Press, 105–110 p.

Wyllie, P.J., 1980, The origin of kimberlite: Journal of Geophysical Research, v. 85, p. 6902, doi:10.1029/JB085iB12p06902.